


Review

A Beginner's Guide to Thermodynamic Modelling of [FeFe] Hydrogenase

James A. Birrell ^{1,*} , Patricia Rodríguez-Maciá ^{2,*} and Adrian Hery-Barranco ²

¹ Max Planck Institute for Chemical Energy Conversion, Stiftstraße 34-36, 45470 Mülheim an der Ruhr, Germany

² Inorganic Chemistry Laboratory, University of Oxford, South Parks Road, Oxford OX1 3QR, UK; adrian.herybarranco@chem.ox.ac.uk

* Correspondence: james.birrell@cec.mpg.de (J.A.B.); patricia.rodriguezmacia@chem.ox.ac.uk (P.R.-M.)

Abstract: [FeFe] hydrogenases, which are considered the most active naturally occurring catalysts for hydrogen oxidation and proton reduction, are extensively studied as models to learn the important features for efficient H₂ conversion catalysis. Using infrared spectroscopy as a selective probe, the redox behaviour of the active site H-cluster is routinely modelled with thermodynamic schemes based on the Nernst equation for determining thermodynamic parameters, such as redox midpoint potentials and *pK_a* values. Here, the thermodynamic models usually applied to [FeFe] hydrogenases are introduced and discussed in a pedagogic fashion and their applicability to additional metalloenzymes and molecular catalysts is also addressed.

Keywords: hydrogenase; modelling; thermodynamics; infrared spectroscopy; redox; metalloenzymes



Citation: Birrell, J.A.;

Rodríguez-Maciá, P.; Hery-Barranco, A.

A Beginner's Guide to Thermodynamic Modelling of [FeFe] Hydrogenase.

Catalysts **2021**, *11*, 238. [https://](https://doi.org/10.3390/catal11020238)

doi.org/10.3390/catal11020238

Academic Editor: Marius Horch

Received: 21 January 2021

Accepted: 7 February 2021

Published: 11 February 2021

Publisher's Note: MDPI stays neutral with regard to jurisdictional claims in published maps and institutional affiliations.



Copyright: © 2021 by the authors. Licensee MDPI, Basel, Switzerland. This article is an open access article distributed under the terms and conditions of the Creative Commons Attribution (CC BY) license (<https://creativecommons.org/licenses/by/4.0/>).

1. Introduction

Hydrogen is considered as a possible fuel for the future due to its high energy density and efficient combustion that produces only water as a waste product [1]. However, to date, the most efficient industrial catalysts for H₂ fuel cells as well as for water electrolysis use rare and expensive noble metals such as platinum, palladium, and rhodium. Thus, discovering new catalysts based on earth abundant metals, is an intensive area of research. In order to find inspiration, natural biological catalysts called enzymes are investigated, which use abundant metals like iron and nickel with a similar efficiency to platinum [2–4]. [FeFe] hydrogenases have been in the spotlight in recent years [5–7] due to their high efficiency and activity for H₂ oxidation and H⁺ reduction compared with their less active [NiFe] counterparts. For a long time, the major drawback of [FeFe] hydrogenases was their oxygen sensitivity [8–10]. However, methods that have recently been identified can protect these enzymes for later use [11–14], and even enzymes with a self-protection mechanism have been discovered [15,16].

[FeFe] hydrogenases have an intriguing active site named the H-cluster (for H₂ converting cluster, Figure 1A,B), which is composed of a canonical [4Fe-4S] cluster, tightly ligated to the protein through the thiolate groups of four cysteine amino acids [17,18]. One of these thiolates bridges to a unique diiron subcluster, which is decorated with a terminal cyanide (CN[−]) and carbon monoxide (CO) ligand on each iron as well as a CO and a 2-azapropane-1,3-dithiolate (ADT) ligand bridging the two iron ions [19]. The strong field ligands CN[−] and CO ensure the iron ions are in low oxidation states (Fe²⁺ and Fe⁺), as well as in low spin states (*S* = 0 and *S* = 1/2). Furthermore, the protein environment forces an open coordination site on the iron furthest from the [4Fe-4S] cluster. This low valent Fe site behaves as a Lewis acid, while the nitrogen bridgehead atom of the dithiolate ligand behaves as a base, which protonates around neutral pH. Together, they form a frustrated Lewis pair, ideally placed to heterolytically split H₂. The low valent Fe stabilises the terminal hydride and the nitrogen bridgehead accepts the proton [20–24].

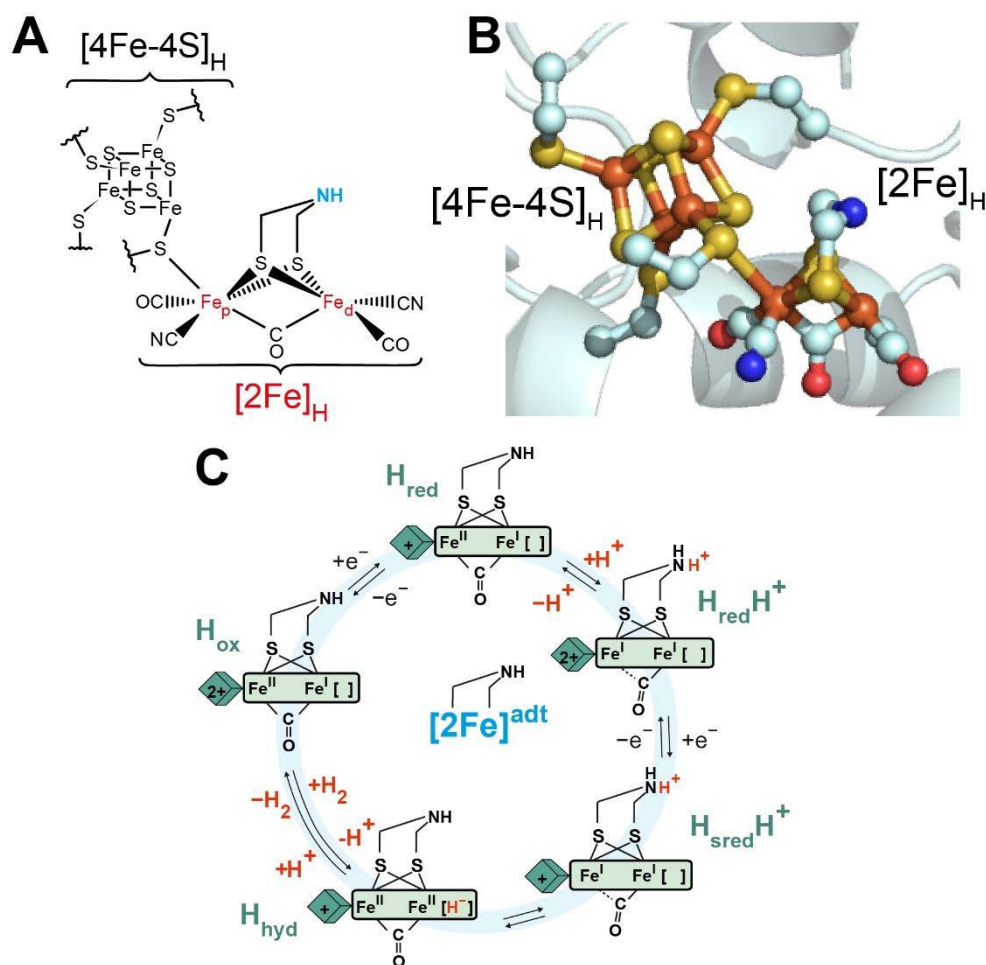


Figure 1. Structure and catalytic cycle of [FeFe] hydrogenase. (A) Structure of the H-cluster. (B) Structure of CrHydA1 apo protein (PDB ID 3LX4) [25] with the H-cluster modelled in from the CpHydA1 structure (PDB ID 4XDC) [26]. The H-cluster is composed of the [4Fe-4S]_H and [2Fe]_H subclusters and is shown in the balls and sticks representation, along with the cysteines ligating [4Fe-4S]_H. (C) Simple form proposed for the catalytic cycle, where [4Fe-4S]_H is represented by a diamond and [2Fe]_H is represented as a rectangle. The CN⁻ and terminal CO ligands are omitted for clarity. Recent work from Lorent and coworkers has uncovered additional forms of the H_{hyd} state [27].

The mechanism of the [FeFe] hydrogenases has been intensively studied and is heatedly discussed with a number of possible models available based on results arising from a range of different types of experiments [28–30]. One of the most routinely applied techniques has been infrared (IR) spectro-electrochemistry. The main reason for this is that [FeFe] hydrogenases have active sites containing the π -acid ligands CO and CN⁻, which are excellent IR probe reporters [31]. The vibrational frequencies of these ligands appear in a range of the mid-IR that is free from other vibrations occurring in the protein. Even more importantly, these metal bound ligands are very sensitive to changes in the oxidation state of the metal. As such, IR spectroscopy is an ideal tool for investigating the oxidation state of both the [4Fe-4S] and [2Fe] parts of the active site of [FeFe] hydrogenase with applied potential under a range of conditions. For example, IR spectro-electrochemical experiments can be performed at various pH values [32–36], adding external inhibitors [37,38], or by using different forms of the enzyme where catalysis is altered by chemical modifications to the active site metallocofactor or the nearby amino acids [34,36,38]. One of the most important modifications in this regard was the change of the natural ADT ligand to propane-1,3-dithiolate (PDT), which contains a methylene group instead of the amino group in the bridgehead. The PDT ligand can, therefore, not be protonated at the bridgehead atom, rendering the [2Fe]_H subcluster redox silent, allowing us to focus on the electron transfer

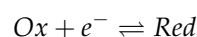
processes at the $[4\text{Fe-4S}]_{\text{H}}$ subcluster [38]. These studies have then been interpreted using thermodynamic (and sometimes kinetic) models in order to try and learn what factors make catalysis so efficient, and lead to the development of models for the catalytic cycle (Figure 1C).

In this review, we try to build up a simple thermodynamic model for the behaviour of the H-cluster, starting from the simple Nernst equation describing a one-electron redox event and the acid dissociation constant describing a de-protonation event independently (Section 2.1). We then combine these two events to generate a proton-coupled electron transfer model (Section 2.2). After that, in Section 2.3, we combine two redox steps with a protonation step to create a basic model describing the main states observed in $[\text{FeFe}]$ hydrogenase. We also consider the involvement of accessory iron-sulfur clusters that interact through redox anti-cooperativity (Section 2.4). Finally, we combine redox anti-cooperativity with the basic H-cluster model to describe the unusual behaviour of an F-cluster containing $[\text{FeFe}]$ hydrogenase (Section 2.5). These models are then discussed in the context of $[\text{FeFe}]$ hydrogenase research and an example of how one of these thermodynamic models was employed in practice is given. We also address how these models could be extended to look at even more complex situations and how they could be applied to other enzymes. For those who are interested, all the models presented in this review are available as a supplementary spreadsheet Models.xlsx from the MDPI website.

2. Thermodynamic Modelling of $[\text{FeFe}]$ Hydrogenase

2.1. The Basics

The first stage of building up a thermodynamic model is to consider the simplest system possible. This is a system with a single redox cofactor that engages in reduction or oxidation by a single electron.



This simple system could be used to describe an iron-sulfur cluster in a ferredoxin or the H-cluster in $[\text{FeFe}]$ hydrogenase matured with a $[2\text{Fe}]$ precursor containing PDT. The latter has been argued to have a pH dependent redox potential [36]. However, provided that we do not change the pH of the redox titration, this simple one-electron redox model is sufficient. This simple redox couple is described by the well-known Nernst equation [39]. Assuming that the activity coefficients of the species *Ox* and *Red* approach 1 (a valid assumption when dealing with low concentrations as is the case for experiments with enzymes), the activity can be approximated with concentrations.

$$E = E^O - \frac{RT}{nF} \ln \left(\frac{[\text{Red}]}{[\text{Ox}]} \right) \quad (1)$$

where E is the applied potential in V vs. the Standard Hydrogen Electrode (SHE), E^O is the standard redox potential of the *Ox/Red* couple in V vs. SHE, R is the molar gas constant ($8.314 \text{ J K}^{-1} \text{ mol}^{-1}$), T is the temperature in K, n is the number of electrons transferred (in this case $n = 1$), F is the Faraday constant ($96,485 \text{ C mol}^{-1}$), and $[\text{Red}]$ and $[\text{Ox}]$ are the concentrations of the reduced and oxidised species in M units, respectively.

To find how the species *Ox* and *Red* vary with the potential they experience (this can either be from an electrode, or from a chemical redox couple, e.g., $2\text{H}^+/\text{H}_2$ in the case of hydrogenase), we need to rearrange the Nernst equation and define the total concentration of both *Ox* and *Red*. Throughout this review, we will define the sum of the concentration of the involved species as 1 (when dealing with real concentrations of the enzyme, the fraction in a given state will need to be scaled to the total concentration). Therefore:

$$\begin{aligned} [\text{Ox}] + [\text{Red}] &= 1 \\ [\text{Red}] &= 1 - [\text{Ox}] \end{aligned} \quad (2)$$

Rearranging the Nernst Equation (1), we get:

$$[Red] = [Ox] \times \exp \frac{nF}{RT} (E^O - E)$$

Substituting $[Red]$ with (2), we get:

$$(1 - [Ox]) = [Ox] \times \exp \frac{nF}{RT} (E^O - E)$$

$$1 = [Ox] + [Ox] \times \exp \frac{nF}{RT} (E^O - E)$$

$$1 = [Ox] \left\{ 1 + \exp \frac{nF}{RT} (E^O - E) \right\}$$

$$[Ox] = \frac{1}{1 + \exp \frac{nF}{RT} (E^O - E)} \quad (3)$$

Plotting $[Ox]$ (Equation (3)) and $[Red]$ (Equation (2)) against the applied potential using an E^O value of -400 mV vs. SHE (chosen as an arbitrary potential close to the thermodynamic potential of the $2H^+/H_2$ couple at physiological pH) and $n = 1$ (indicating a single electron transferred), it then gives the curves shown in Figure 2. It can clearly be seen that, at a high applied potential (-200 mV) Ox dominates, and, as the applied potential decreases, Ox is converted gradually to Red with a middle point (the midpoint potential) of -400 mV.

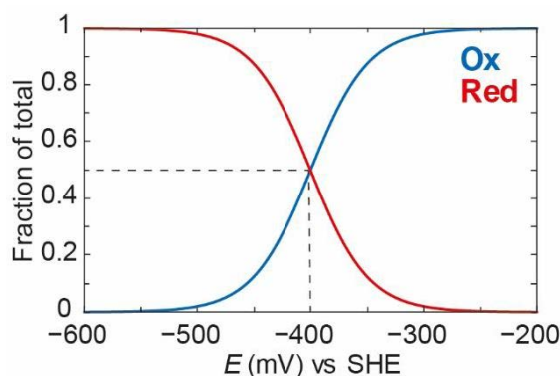
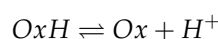


Figure 2. Variation of the fraction of oxidised (Ox , blue) and reduced (Red , red) species as a function of the applied potential (E) in mV. The curves were obtained using Equations (2) and (3) with $n = 1$ and $E^O = -400$ mV vs. SHE.

Next, instead of assuming a redox event, we will assume a deprotonation event of a single cofactor with a single proton.



This situation is explained nicely by a simple acid dissociation constant (K_a):

$$K_a = \frac{[Ox][H^+]}{[OxH]} \quad (4)$$

where K_a is the acid dissociation constant, $[Ox]$ is the concentration of the deprotonated species, $[H^+]$ is the concentration of protons, and $[OxH]$ is the concentration of the protonated species in M units.

$$[Ox] + [OxH] = 1$$

$$[OxH] = 1 - [Ox] \quad (5)$$

Rearranging Equation (4), we get:

$$K_a[\text{OxH}] = [\text{Ox}][\text{H}^+]$$

$$[\text{OxH}] = [\text{Ox}] \frac{[\text{H}^+]}{K_a}$$

Then $[\text{OxH}]$ is substituted with Equation (5):

$$1 - [\text{Ox}] = [\text{Ox}] \frac{[\text{H}^+]}{K_a}$$

$$1 = [\text{Ox}] + [\text{Ox}] \frac{[\text{H}^+]}{K_a}$$

$$1 = [\text{Ox}] \left(1 + \frac{[\text{H}^+]}{K_a}\right)$$

$$[\text{Ox}] = \frac{1}{1 + \frac{[\text{H}^+]}{K_a}}$$

Finally, this can be rearranged to express $[\text{Ox}]$ in terms of the difference between the pK_a and the pH:

$$pK_a = -\log_{10}(K_a)$$

$$\text{pH} = -\log_{10}([\text{H}^+])$$

$$K_a = 10^{-pK_a}$$

$$[\text{H}^+] = 10^{-\text{pH}}$$

$$[\text{Ox}] = \frac{1}{1 + \frac{10^{-\text{pH}}}{10^{-pK_a}}}$$

$$[\text{Ox}] = \frac{1}{1 + 10^{(\text{pH} - \text{p}K_a)}} \quad (6)$$

Plotting $[\text{Ox}]$ (Equation (6)) and $[\text{OxH}]$ (Equation (5)) against the pH using a K_a value of 10^{-7} (or a pK_a of 7) gives the curves shown in Figure 3. At a high pH, the deprotonated species Ox dominates, and, as the pH decreases, Ox converts gradually to OxH with a pK_a of 7.

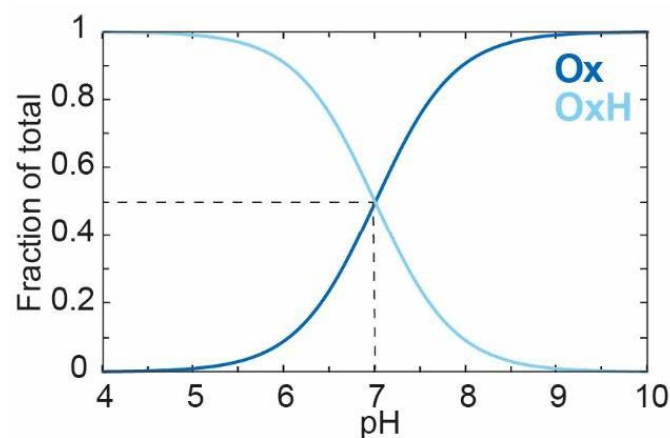
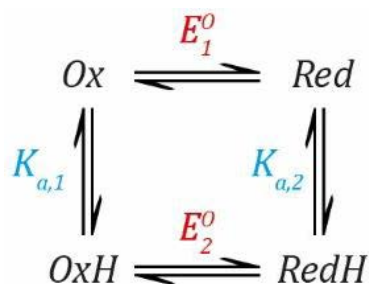


Figure 3. Variation of the fraction (out of 1) of deprotonated (Ox , dark blue) and protonated (OxH , light blue) species as a function of the pH. The curves were obtained using Equations (5) and (6) for an acid dissociation constant and a pK_a value of 7.

2.2. Proton Coupled Electron Transfer

Now, we can combine both events into a thermodynamic model describing a species that can be protonated and reduced by one electron simultaneously, as shown in Scheme 1.



Scheme 1. Scheme showing the reactions in a simple proton coupled electron transfer (PCET) process. The oxidised and deprotonated species *Ox* can be reduced to *Red* with a redox potential of E_1^O . The oxidised and protonated species *OxH* can be reduced to give *RedH* with a redox potential of E_2^O . *OxH* can be deprotonated to *Ox* with an acid dissociation constant $K_{a,1}$. *RedH* can be deprotonated to give *Red* with an acid dissociation constant $K_{a,2}$.

Now, we need to define two E^O values based on the Nernst Equation (1), including one for the deprotonated states (*Ox* and *Red*) and one for the protonated states (*OxH* and *RedH*), and two K_a values based on the simple acid dissociation constant Equation (4), one for the oxidised states (*Ox* and *OxH*) and one for the reduced states (*Red* and *RedH*). Here, as before, E refers to the applied potential to the system and, therefore, all redox couples are in equilibrium with this.

$$E = E_1^O - \frac{RT}{nF} \ln \left(\frac{[Red]}{[Ox]} \right)$$

$$E = E_2^O - \frac{RT}{nF} \ln \left(\frac{[RedH]}{[OxH]} \right)$$

$$K_{a,1} = \frac{[Ox][H^+]}{[OxH]}$$

$$K_{a,2} = \frac{[Red][H^+]}{[RedH]}$$

These equations can be rearranged to get everything in terms of $[Ox]$ as follows.

$$[Red] = [Ox] \times \exp \frac{nF}{RT} (E_1^O - E)$$

$$[Red] = [Ox] \times \alpha \quad (7)$$

where:

$$\alpha = \exp \frac{nF}{RT} (E_1^O - E) \quad (8)$$

$$[RedH] = [OxH] \times \exp \frac{nF}{RT} (E_2^O - E)$$

$$[RedH] = [OxH] \times \beta \quad (9)$$

where:

$$\beta = \exp \frac{nF}{RT} (E_2^O - E) \quad (10)$$

$$[OxH] = [Ox] \frac{[H^+]}{K_{a,1}} \quad (11)$$

$$[RedH] = [Red] \frac{[H^+]}{K_{a,2}} \quad (12)$$

Again, we define the sum of the concentration of all states as 1.

$$[Ox] + [Red] + [OxH] + [RedH] = 1 \quad (13)$$

Next, we substitute $[OxH]$ and $[RedH]$ from Equations (11) and (12) into Equation (13).

$$\begin{aligned} [Ox] + [Red] + [Ox] \frac{[H^+]}{K_{a,1}} + [Red] \frac{[H^+]}{K_{a,2}} &= 1 \\ [Ox] + [Ox] \frac{[H^+]}{K_{a,1}} + [Red] + [Red] \frac{[H^+]}{K_{a,2}} &= 1 \\ [Ox] \left(1 + \frac{[H^+]}{K_{a,1}}\right) + [Red] \left(1 + \frac{[H^+]}{K_{a,2}}\right) &= 1 \end{aligned} \quad (14)$$

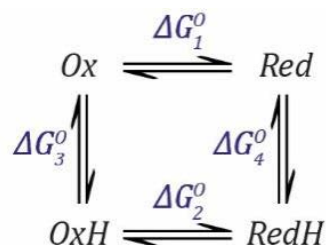
followed by substitution of $[Red]$ from Equation (7) into Equation (14).

$$\begin{aligned} [Ox] \left(1 + \frac{[H^+]}{K_{a,1}}\right) + [Ox] \times \alpha \left(1 + \frac{[H^+]}{K_{a,2}}\right) &= 1 \\ [Ox] \left\{1 + \frac{[H^+]}{K_{a,1}} + \alpha \left(1 + \frac{[H^+]}{K_{a,2}}\right)\right\} &= 1 \\ [Ox] &= \frac{1}{1 + \frac{[H^+]}{K_{a,1}} + \alpha \left(1 + \frac{[H^+]}{K_{a,2}}\right)} \end{aligned}$$

As for Equation (6) from Section 2.1, this can be rearranged to express $[H^+]$, $K_{a,1}$, and $K_{a,2}$ as pH , $pK_{a,1}$, and $pK_{a,2}$.

$$[Ox] = \frac{1}{1 + 10^{(pK_{a,1}-pH)} + \alpha(1 + 10^{(pK_{a,2}-pH)})} \quad (15)$$

Importantly, in order to arrive at this result, we only need to consider the two protonation events defined by $K_{a,1}$ and $K_{a,2}$ and the reduction event defined by E_1^O . We can calculate E_2^O by considering that the free energy change (ΔG) when going from Ox to $RedH$ is the same, whether we go via Red or via OxH . We can define the situation (Scheme 2) as follows (remember that $K_{a,1}$ and $K_{a,2}$ are dissociation constants, so the free energy change ΔG is defined for this direction and must be subtracted when we go in the opposite direction).



Scheme 2. Scheme showing the free energy changes for the reactions in a simple proton coupled electron transfer (PCET) process. The oxidised and deprotonated species Ox can be reduced to Red with a free energy change ΔG_1 . The oxidised and protonated species OxH can be reduced to give $RedH$ with a free energy change ΔG_2 . OxH and $RedH$ can be deprotonated to Ox and Red , respectively, with free energy changes ΔG_3 and ΔG_4 , respectively ($-\Delta G_3$ and $-\Delta G_4$ for the respective protonation processes).

The total free energy change when going from *Ox* to *RedH* is the same whether we go via *Red* or *OxH* (ΔG_3^O and ΔG_4^O are subtracted because they are defined for the deprotonation process).

$$\Delta G_1^O - \Delta G_4^O = \Delta G_2^O - \Delta G_3^O \quad (16)$$

Since:

$$\Delta G = -nFE$$

$$\Delta G = -RT \ln K$$

we can define the free energy changes for the reduction and deprotonation steps as follows.

$$\Delta G_1^O = -nFE_1^O \quad (17)$$

$$\Delta G_2^O = -nFE_2^O \quad (18)$$

$$\Delta G_3^O = -RT \ln K_{a,1} \quad (19)$$

$$\Delta G_4^O = -RT \ln K_{a,2} \quad (20)$$

which can then be substituted into Equation (16) and rearranged for E_2^O .

$$\begin{aligned} -nFE_1^O - (-RT \ln K_{a,2}) &= -nFE_2^O - (-RT \ln K_{a,1}) \\ -nFE_1^O + RT \ln K_{a,2} &= -nFE_2^O + RT \ln K_{a,1} \\ nFE_2^O &= nFE_1^O + RT \ln K_{a,1} - RT \ln K_{a,2} \\ E_2^O &= E_1^O + \frac{RT}{nF} \ln \frac{K_{a,1}}{K_{a,2}} \end{aligned} \quad (21)$$

Using this simple model, we can plot the dependence of each of the species *Ox*, *Red*, *OxH*, and *RedH* as a function of either the applied potential at a given pH (Figure 4A) or as a function of the pH at a given applied potential (Figure 4B).

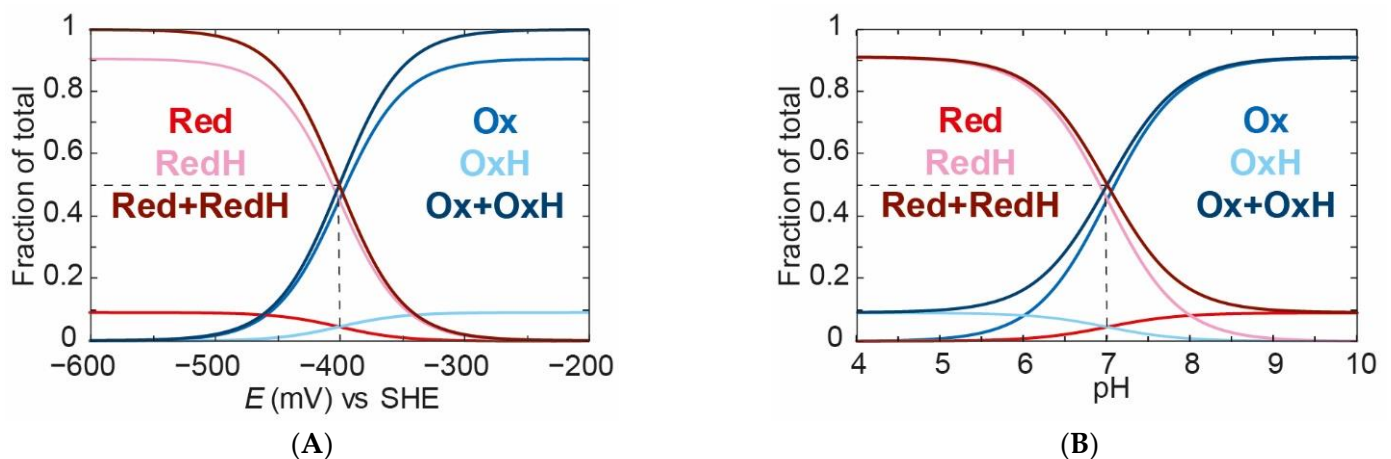


Figure 4. Variation of the fraction (out of 1) of deprotonated oxidised (*Ox*, medium blue), deprotonated reduced (*Red*, medium red), protonated oxidised (*OxH*, light blue), and protonated reduced (*RedH*, light red) species as a function of the applied potential (A) and pH (B). The sum of *Ox* and *OxH* (dark blue) and the sum of *Red* and *RedH* (dark red) are also plotted. The curves were obtained using Equations (7), (11), (12), and (15), with $E_1^O = -459$ mV vs. SHE, $K_{a,1} = 10^{-6}$ ($pK_{a,1} = 6$), $K_{a,2} = 10^{-8}$ ($pK_{a,2} = 8$), and a pH of 7 (A) or an applied potential of -400 mV vs. SHE (B). These values are arbitrary, but were chosen here to give conditions where significant PCET can be observed with an apparent redox midpoint potential of -400 mV and an apparent pK_a value of 7. E_2^O was calculated using Equation (21) to be -341 mV, giving an average E^O of -400 mV vs. SHE, for a comparison with Figure 2.

We can see that, at a fixed pH value of 7 (Figure 4A), when we titrate the applied potential from high (less negative) to low (more negative), we go from about 90% *Ox* and 10% *OxH* to about 10% *Red* and 90% *RedH*. A crucial observation needs to be made at this stage: all species titrate with an identical “apparent” midpoint potential of -400 mV. This is because the redox and protonation events are coupled. Importantly, the *Ox*:*OxH* ratio and the *Red*:*RedH* ratio do not change with the applied potential. This may seem clear, but a lack of understanding of this concept could lead to erroneous conclusions.

Similarly, if we titrate the pH from high to low at a constant applied potential of -400 mV (Figure 4B), we can see that we go from a mixture of 90% *Ox* and 10% *Red* to a mixture of 10% *OxH* and 90% *RedH* with an “apparent” pK_a of 7. This is an important observation in which we have shown that the redox state is dependent on the pH. This indicates the presence of a proton coupled electron transfer (PCET). The reason for this is that we have chosen different pK_a values for the oxidised and reduced species. If we had identical pK_a values for the oxidised and reduced species, then no PCET would occur. This situation is shown in Figure 5A,B, where the pK_a values are both 7. Since the applied potential is titrated from high to low, a 50% mixture of *Ox* and *OxH* converts to a 50% mixture of *Red* and *RedH* with an “apparent” midpoint potential of -400 mV vs. SHE. In Figure 5B, the total oxidised species (*Ox* + *OxH*) to the total reduced species (*Red* + *RedH*) ratio does not change with pH, indicating no PCET. However, it can be seen that *Ox* titrates to *OxH* and *Red* titrates to *RedH* as the pH is changed from high to low.

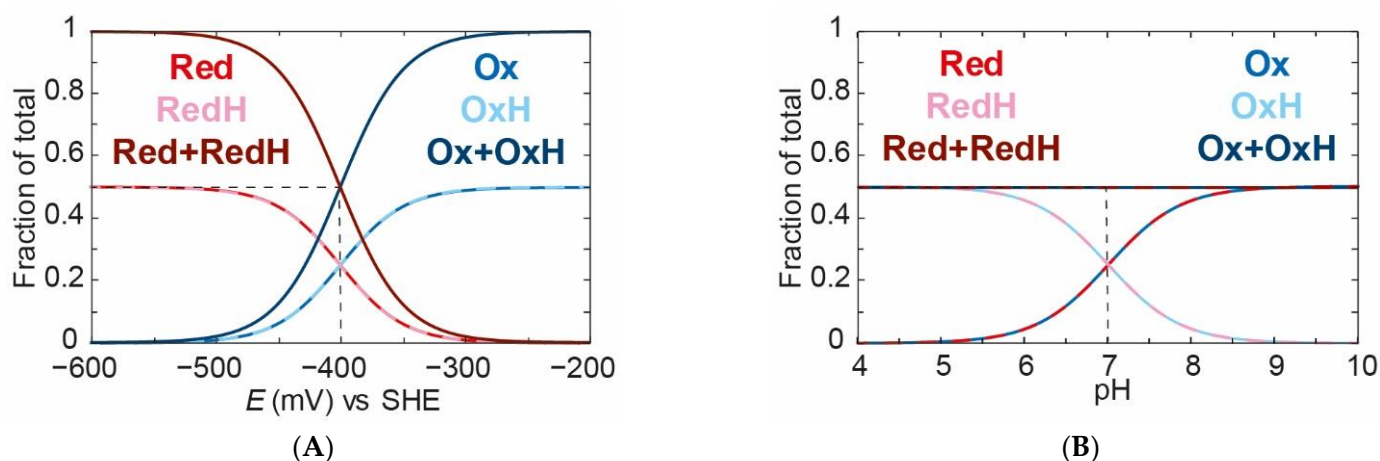


Figure 5. Variation of the fraction (out of 1) of deprotonated oxidised (*Ox*, medium blue), deprotonated reduced (*Red*, medium red), protonated oxidised (*OxH*, light blue dashed), and protonated reduced (*RedH*, light Red dashed) species as a function of the applied potential (A) or pH (B). The sum of *Ox* and *OxH* (dark blue) and the sum of *Red* and *RedH* (dark red) are also plotted. The curves were obtained using Equations (7), (11), (12), and (15), with $E_1^O = -400$ mV, $K_{a,1} = K_{a,2} = 10^{-7}$ ($pK_{a,1} = pK_{a,2} = 7$), a pH of 7 (A) or an applied potential of -400 mV vs. SHE (B). These values are arbitrary, but were chosen here to give conditions where no PCET can be observed but conserve the redox midpoint potential of -400 mV and apparent pK_a value of 7. E_2^O was calculated using Equation (21) to be -400 mV, giving an average E^O of -400 mV, for a comparison with Figure 2.

To emphasise the crucial observation that “apparent” redox potentials can shift with pH for the case where we have different pK_a values for *Ox* and *Red*, one can compare the titrations of the *Ox* species at three pH values (Figure 6).

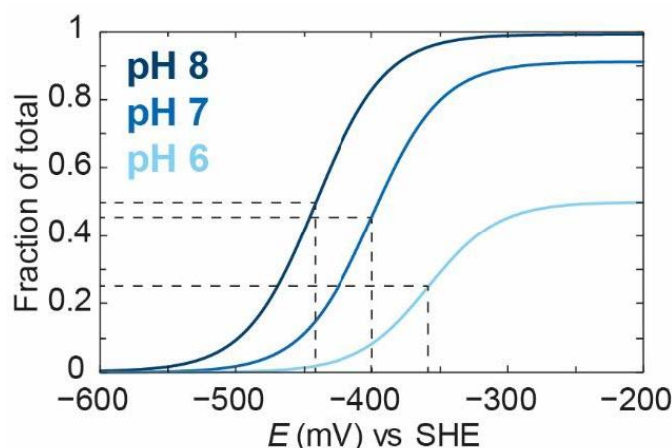


Figure 6. Variation of the fraction (out of 1) of deprotonated oxidised (*Ox*) species as a function of the applied potential at pH 6 (light blue), pH 7 (medium blue), and pH 8 (dark blue). The curves were obtained using Equations (7), (11), (12), and (15), with $E_1^O = -459$ mV, $K_{a,1} = 10^{-6}$ ($pK_{a,1} = 6$), $K_{a,2} = 10^{-8}$ ($pK_{a,2} = 8$). E_2^O was calculated using Equation (21) to be -341 mV, giving an average E^O of -400 mV, for a comparison with Figure 2.

As can be seen from Figure 6, the “apparent” midpoint potential for the titration of *Ox* shifts with pH, even if the change of *Ox* to *Red* itself does not directly involve a proton. However, the fundamental point is that the ratio between the *Ox* and *OxH* species will be the same at every value of the applied potential (as long as the pH is fixed). This is because the ratio between *Ox* and *OxH* is determined only by the acid dissociation constant $K_{a,1}$. Thus, if the process of proton-coupled reduction of *Ox* to *RedH* can occur, then the titration of the total amount of the oxidised species (*Ox* + *OxH*) and the titration of the total amount of the reduced species (*Red* + *RedH*), will change with pH. It must, therefore, be the case that the titration of the component states changes with pH. To illustrate this, Figure 7 shows the titration of *Ox*, *OxH*, and *Ox* + *OxH* at pH 6 and pH 8. It is clear that, at pH 6, the *Ox* state titrates with a more positive “apparent” redox potential than at pH 8. The components *Ox* and *OxH* species titrate with the same potential at pH 6. At pH 8, only the *Ox* state can be observed since its pK_a is too low to observe *OxH* at this pH.

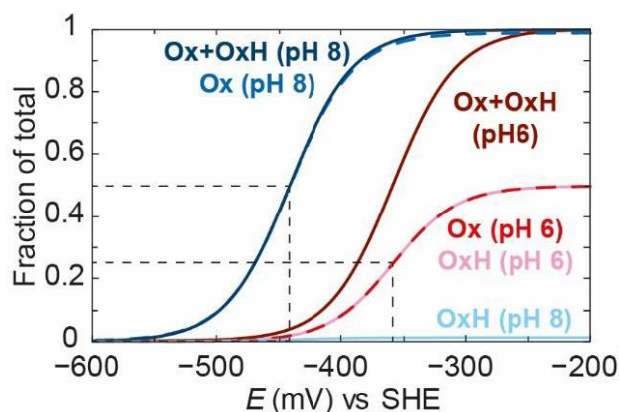


Figure 7. Variation of the fraction (out of 1) of the total oxidised (*Ox* + *OxH*, dark blue/red), the deprotonated oxidised (*Ox*, dashed blue/red), and the protonated oxidised (*OxH*, light blue/red) species as a function of the applied potential at pH 6 (red) and pH 8 (blue). The curves were obtained using Equations (7), (11), (12), and (15), with $E_1^O = -459$ mV, $K_{a,1} = 10^{-6}$ ($pK_{a,1} = 6$), and $K_{a,2} = 10^{-8}$ ($pK_{a,2} = 8$). E_2^O was calculated using Equation (21) to be -341 mV, giving an average E^O of -400 mV, for a comparison with Figure 2.

Using the E_1^O , E_2^O , $pK_{a,1}$, and $pK_{a,2}$ values defined in Figure 4, for a PCET process, we can plot the famous Pourbaix diagram [40] in which the regions of stability of each of the species *Ox*, *OxH*, *Red*, and *RedH* are defined (Figure 8). It should be recognised, however, that the boundaries between each of these regions do not represent step functions but represent the smooth titrations between each state. For example, it can be seen in Figure 4 that, at pH 7 and $E = -400$ mV (a point right in the middle of the Pourbaix diagram in Figure 8), we have about 45% *Ox*, 45% *RedH*, 5% *OxH*, and 5% *Red*. Thus, we still observe *OxH* and *Red* even though we are outside of the regions where these states are defined as stable in the Pourbaix diagram.

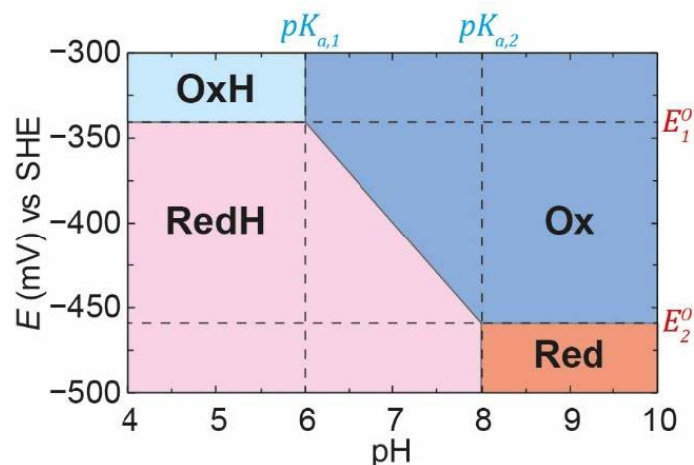


Figure 8. The Pourbaix diagram indicating the regions of relative stability of the species *Ox*, *OxH*, *Red*, and *RedH* with pH and applied potential (E). The values of the constants defining the regions of the diagram are the same as those used in Figure 4: $E_1^O = -459$ mV, $K_{a,1} = 10^{-6}$ ($pK_{a,1} = 6$), $K_{a,2} = 10^{-8}$ ($pK_{a,2} = 8$). E_2^O was calculated to be -341 mV, giving an average E^O of -400 mV. The areas of the diagram are coloured to indicate the regions where *Ox* (dark blue), *OxH* (light blue), *Red* (dark red), and *RedH* (light red) dominate.

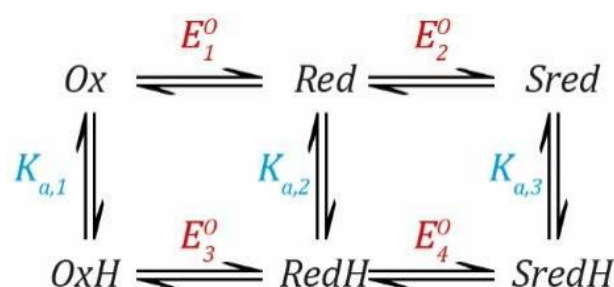
2.3. A Simple Model for the [FeFe] Hydrogenase

Experimental data show that the simplest [FeFe] hydrogenase, *CrHydA1*, containing only the H-cluster and no additional F-clusters, can be reduced by two electrons. The most oxidised state H_{ox} gets reduced by one electron to form H_{red} , and H_{red} can subsequently be reduced by a second electron to yield H_{sred} [41,42].



It was shown that photoexcitation of frozen samples of the H_{red} state gave a different form of H_{red} , which was named H_{red}' [43]. Around the same time, it was noted that H_{red}' dominated at high pH, while H_{red} dominated at low pH [35]. Furthermore, it was observed that only the H_{red}' state formed in the PDT variant of *CrHydA1* (which lacks a protonatable dithiolate ligand in $[2Fe]_H$) [38]. The simplest interpretation of the data was that the electron could reside mostly on the $[4Fe-4S]_H$ subcluster, or mostly on the $[2Fe]_H$ subcluster, and that protonation of the ADT bridging nitrogen from NH to NH_2^+ was the event that triggered the electronic rearrangement. Thus, the H_{red}' and H_{red} states were renamed H_{red} and $H_{red}H^+$, respectively [35]. Moreover, based on the fact that H_{sred} cannot be formed in the PDT variant of *CrHydA1* [38], it was assumed that H_{sred} should be in a protonated state, and was named $H_{sred}H^+$. To describe this situation, a more complex model is required including two redox steps and one protonation step.

In Section 2.2, we described a simple model for proton coupled electron transfer in which four states exist: *Ox*, *OxH*, *Red*, and *RedH*. Now, we will extend this model to include a second redox event (Scheme 3).



Scheme 3. Scheme showing the reactions in a simple model for the [FeFe] hydrogenase. The oxidised and deprotonated species *Ox* can be reduced to *Red* with a redox potential of E_1^0 . *Red* can then be further reduced to *Sred* with a redox potential of E_2^0 . The oxidised protonated species *OxH* can be reduced to give *RedH* with a redox potential of E_3^0 and *RedH* can be further reduced to give *SredH* with a redox potential of E_4^0 . *OxH*, *RedH*, and *SredH* can be deprotonated to *Ox*, *Red*, and *Sred*, respectively, with acid dissociation constants $K_{a,1}$, $K_{a,2}$, and $K_{a,3}$, respectively.

This creates a total of six states connected by seven steps. In this model, *Ox* is the most oxidised state, *Red* is the one electron reduced state, and *Sred* is the two-electron reduced state or “super-reduced” state. Each of these unprotonated states has a protonated counterpart: *OxH*, *RedH*, and *SredH*. Importantly, nothing about this model indicates the location of redox or (de)protonation events because we have a system that can accept two electrons and one proton. One could also consider a model involving one redox and two (de)protonation events, or even two redox and two (de)protonation events. However, the former does not fit at all with experimentally observed spectro-electrochemical titrations, as two redox steps are clearly discerned, while the latter leads to a reactive state that can release H_2 [35,42]. To make a $2e^-/2H^+$ model reversible, an H_2 binding/dissociation step is required, which would complicate the model. Nevertheless, the simple $2e^-/1H^+$ model has been shown to accurately describe pH-dependent spectro-electrochemical titrations [35]. The equations describing this model can be derived using the Nernst Equation (1) and the equation for a simple acid dissociation constant (4) by analogy to those in Section 2.2.

$$\begin{aligned}
 E &= E_1^0 - \frac{RT}{nF} \ln \left(\frac{[Red]}{[Ox]} \right) \\
 E &= E_2^0 - \frac{RT}{nF} \ln \left(\frac{[Sred]}{[Red]} \right) \\
 E &= E_3^0 - \frac{RT}{nF} \ln \left(\frac{[RedH]}{[OxH]} \right) \\
 E &= E_4^0 - \frac{RT}{nF} \ln \left(\frac{[SredH]}{[RedH]} \right) \\
 K_{a,1} &= \frac{[Ox][H^+]}{[OxH]} \\
 K_{a,2} &= \frac{[Red][H^+]}{[RedH]} \\
 K_{a,3} &= \frac{[Sred][H^+]}{[SredH]}
 \end{aligned}$$

As previously done, these equations can be rearranged in terms of $[Ox]$ (for a complete derivation, see the Supplementary Materials Section S1).

$$[Ox] = \frac{1}{1 + \alpha(1 + \beta) + 10^{(pK_{a,1} - pH)} \{1 + \gamma(1 + \delta)\}} \quad (22)$$

where:

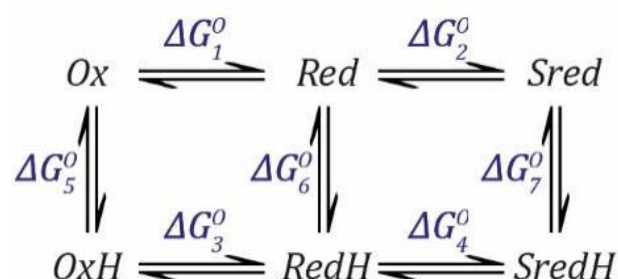
$$\alpha = \exp \frac{nF}{RT} (E_1^O - E) \quad (23)$$

$$\beta = \exp \frac{nF}{RT} (E_2^O - E) \quad (24)$$

$$\gamma = \exp \frac{nF}{RT} (E_3^O - E) \quad (25)$$

$$\delta = \exp \frac{nF}{RT} (E_4^O - E) \quad (26)$$

Although we did not need to use all the parameters to arrive at the results ($K_{a,2}$ and $K_{a,3}$ were not used), we can use the conjoined thermodynamic cycles in this model to derive further equations for these parameters. We can define the situation (Scheme 4) as follows.



Scheme 4. Scheme showing the free energy changes for the reactions in a simple model for the [FeFe] hydrogenase. The oxidised and deprotonated species *Ox* can be reduced to *Red* with a free energy change ΔG_1 . *Red* can be further reduced to *Sred* with a free energy change ΔG_2 . The oxidised protonated species *OxH* can be reduced to give *RedH* with a free energy change ΔG_3 . *RedH* can be further reduced to *SredH* with a free energy change ΔG_4 . *OxH*, *RedH*, and *SredH* can be deprotonated to *Ox*, *Red*, and *Sred*, respectively, with free energy changes ΔG_5 , ΔG_6 , and ΔG_7 , respectively ($-\Delta G_5$, $-\Delta G_6$, and $-\Delta G_7$ for the respective protonation processes).

The rules still apply so that the free energy change is the same regardless which pathway is taken. Thus, going from *Ox* to *RedH* via *Red* or via *OxH* have the same overall free energy change, as does going from *Red* to *SredH* via *Sred* or via *RedH*. Therefore, we can define the following equations.

$$\Delta G_1^O - \Delta G_6^O = \Delta G_3^O - \Delta G_5^O$$

$$\Delta G_2^O - \Delta G_7^O = \Delta G_4^O - \Delta G_6^O$$

where:

$$\Delta G_1^O = -nFE_1^O$$

$$\Delta G_2^O = -nFE_2^O$$

$$\Delta G_3^O = -nFE_3^O$$

$$\Delta G_4^O = -nFE_4^O$$

$$\Delta G_5^O = -RT \ln K_{a,1}$$

$$\Delta G_6^O = -RT \ln K_{a,2}$$

$$\Delta G_7^O = -RT \ln K_{a,3}$$

These equations can then be combined to find expressions for $K_{a,2}$ and $K_{a,3}$ (see SI Section S1 for complete derivations). The final results are shown here:

$$K_{a,2} = K_{a,1} \exp \left\{ \frac{nF}{RT} (E_1^O - E_3^O) \right\} \quad (27)$$

$$K_{a,3} = K_{a,2} \exp \left\{ \frac{nF}{RT} (E_2^O - E_4^O) \right\} \quad (28)$$

Using this model, the populations of all the states can be varied as a function of applied potential at various pH values (Figure 9). As can be seen from Figure 9A, for pH 7, at a high applied potential, only the *Ox* state exists. The *Ox/OxH* transition has such a low pK_a value (2.5) that, at pH 7, the *OxH* state is essentially completely deprotonated and only *Ox* exists. As the applied potential is decreased, the *Ox* state decreases in population (with an apparent midpoint potential of -350 mV) and the *Red* and *RedH* states come up with roughly equal proportions, reaching a maximum concentration at around -400 mV vs. SHE. In this case, the pK_a for the *Red/RedH* transition is ≈ 7.1 , which is why the amount of *RedH* is slightly higher than that of *Red*. As the applied potential decreases even further, *Red* and *RedH* are both converted to *SredH* (with an apparent midpoint potential of -450 mV). The pK_a for the *Sred/SredH* transition is ≈ 11.6 , which means that the *Sred* state is essentially completely protonated to *SredH* at pH 7.

At pH 6 (Figure 9B) and 8 (Figure 9C), similar behaviour can be observed. At pH 6, the *Ox* state is converted to *Red* and *RedH* with a higher apparent midpoint potential (-300 mV) than at pH 7 (-350 mV). The *Red* state is mostly protonated to *RedH*, and the *Red* and *RedH* states are reduced to *SredH* with a higher apparent midpoint potential (-430 mV) than at pH 7 (-450 mV). At pH 8, the *Ox* state is converted to *Red* and *RedH* with a lower apparent midpoint potential (-370 mV) than at pH 7 (-350 mV). The *RedH* state is mostly deprotonated to *Red*, and the *Red* and *RedH* states are reduced to *SredH* with a lower apparent midpoint potential (-480 mV) than at pH 7 (-450 mV).

In Figure 9D, the behaviours of *Ox* and *SredH* are compared at the three pH values. There is a clear observation that the titrations of both species are affected by pH. This is intuitive because the reduction of *Ox* can occur with or without protonation to give *RedH* and *Red*, respectively, with the former requiring a proton. Likewise, reduction of *Red* to *SredH* requires protonation, while reduction of *RedH* to *SredH* does not. In Figure 9E, the behaviours of *Red* and *RedH* are compared at the three pH values. Again, both species appear to be affected by pH. The appearance of *RedH* and the disappearance of *Red* should be pH dependent. What is possibly less intuitive is that the appearance of *Red* and the disappearance of *RedH* also appear to be pH dependent. This is caused by the fact that *Red* and *RedH* are in an equilibrium set by the $pK_{a,2}$ value and the pH. Thus, whatever happens to *Red* must also apply to *RedH* and vice versa. This means that a simple analysis of how the maximum populations of *Red* and *RedH* shift with pH (see Supplementary Discussion in Reference [36]) could erroneously lead to the conclusion that there are two separate proton coupled electron transfer events, including one to make *Red* and one to make *RedH*. This can be seen even more clearly in Figure 9F, where we have plotted a Pourbaix diagram for this model. Between the limits of the $pK_{a,1}$ (2.5) and $pK_{a,2}$ (7.1), the midpoint potential of *Ox* and *OxH* converting to *Red* and *RedH* is pH dependent. Likewise, between the limits of $pK_{a,2}$ and $pK_{a,3}$, the midpoint potential of *Red* and *RedH* converting to *Sred* and *SredH* is also dependent on pH.

In Figure 9, the pK_a values and intrinsic redox potentials have been set to ensure a situation where the *OxH* state is always deprotonated to *Ox*, while the *Sred* state is always protonated to *SredH* and the intermediate *Red(H)* state is a mixture of the protonated (*RedH*) and deprotonated (*Red*) forms (around physiological pH). This situation appears to most accurately reflect the behaviour of the [FeFe] hydrogenase from *CrHydA1* [35]. In Figure 10, we exemplify how this thermodynamic model was employed by Sommer et al. to fit the IR spectro-electrochemical data obtained for the *CrHydA1* hydrogenase at various pH values [35]. Figure 10A shows typical IR spectra under specific conditions that highlight the main catalytic states: H_{ox} , H_{red} , $H_{red}H^+$, and $H_{sred}H^+$. Figure 10B shows electrochemical titrations of the most dominant IR band in each of these states at pH 6, 7, and 8. It can clearly be seen that, as the pH increases, the titration curves shift to a more negative potential. The $H_{red}H^+$ state becomes less abundant and the H_{red} state becomes more abundant. This behaviour seems very logical and fits the requirements of a reversible

enzyme. Around neutral pH and the thermodynamic $2\text{H}^+/\text{H}_2$ potential, the enzyme is in a roughly equal mixture of both *Red* (H_{red}) and *RedH* (H_{red}H^+) states, maximising the concentrations of both and, thereby, maximising the rates of oxidation of *Red* to *Ox* and reduction of *RedH* to *SredH*. If, instead, we imagine a situation where all redox states are deprotonated and only *Ox*, *Red*, and *Sred* exist, then one expects H_2 oxidation to be efficient, but H^+ reduction will be inefficient. Likewise, if all states are protonated, H^+ reduction is efficient but H_2 oxidation is not.

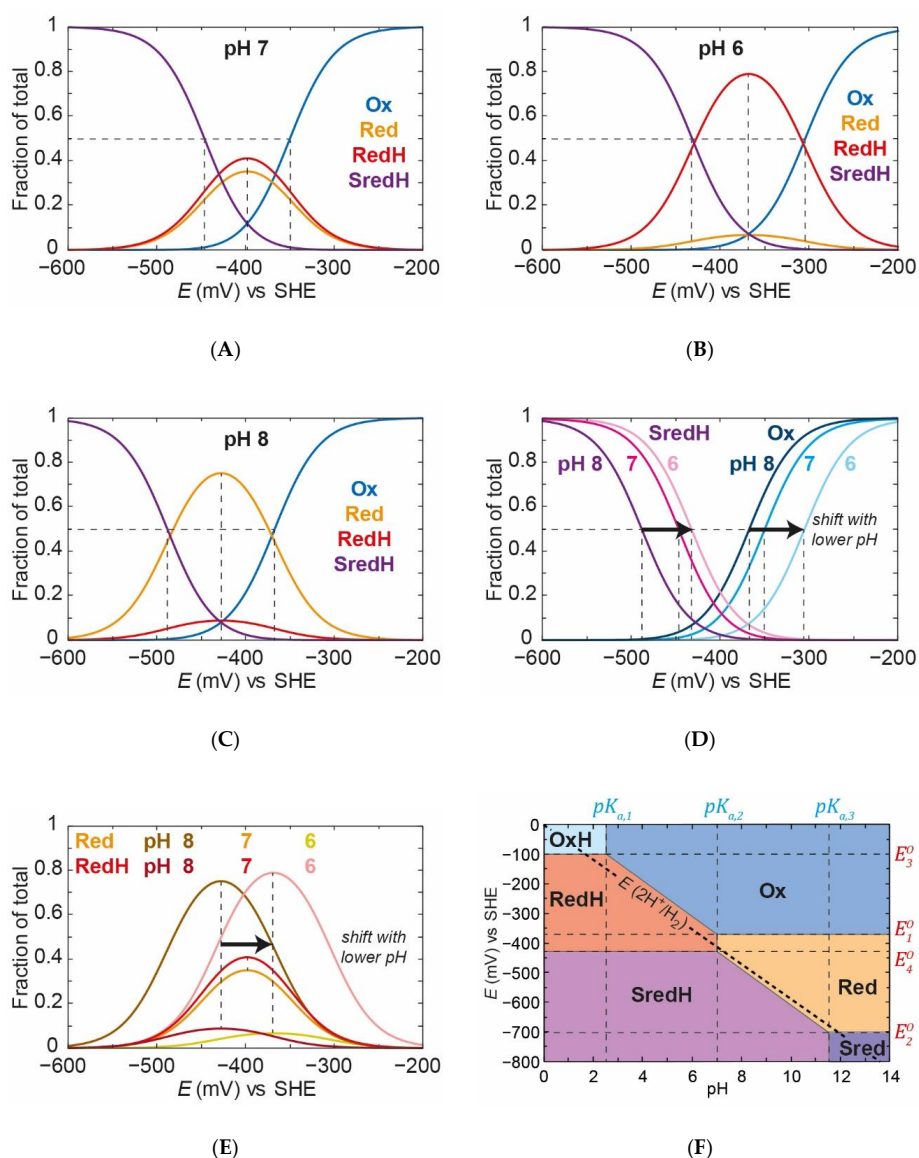


Figure 9. Variation of the fraction (out of 1) of the deprotonated oxidised (*Ox*, blue), deprotonated reduced (*Red*, orange), protonated reduced (*RedH*, red), and protonated super-reduced (*SredH*, purple) species as a function of the applied potential at pH 7 (A), pH 6 (B), and pH 8 (C). The curves were obtained using Equations (22)–(26) with $E_1^O = -370$ mV, $E_2^O = -700$ mV, $E_3^O = -100$ mV, and $E_4^O = -430$ mV, giving an average E^O of -400 mV. For a comparison with previous figures, and $K_{a,1} = 3.16 \times 10^{-3}$ ($pK_{a,1} = 2.5$). $K_{a,2}$ was calculated using Equation (27) to be 8.58×10^{-8} ($pK_{a,2} = 7.1$) and $K_{a,3}$ was calculated using Equation (28) to be 2.33×10^{-12} ($pK_{a,3} = 11.6$). *OxH* and *Sred* are not shown because their concentrations are effectively zero at each pH. (D) *Ox* (blue) and *SredH* (purple) are plotted at pH 6 (light), pH 7 (medium), and pH 8 (dark). (E) *Red* (orange) and *RedH* (red) are plotted at pH 6 (light), pH 7 (medium), and pH 8 (dark). (F) The Pourbaix diagram showing the regions with respect to pH and applied potential (E) where *Ox* (dark blue), *OxH* (light blue), *Red* (orange), *RedH* (red), *Sred* (dark purple), and *SredH* (light purple) dominate, based on the values of E_1^O to E_4^O and $pK_{a,1}$ to $pK_{a,3}$ described above. The thermodynamic potential of the $2\text{H}^+/\text{H}_2$ couple is plotted vs. pH (dotted line) for a comparison.

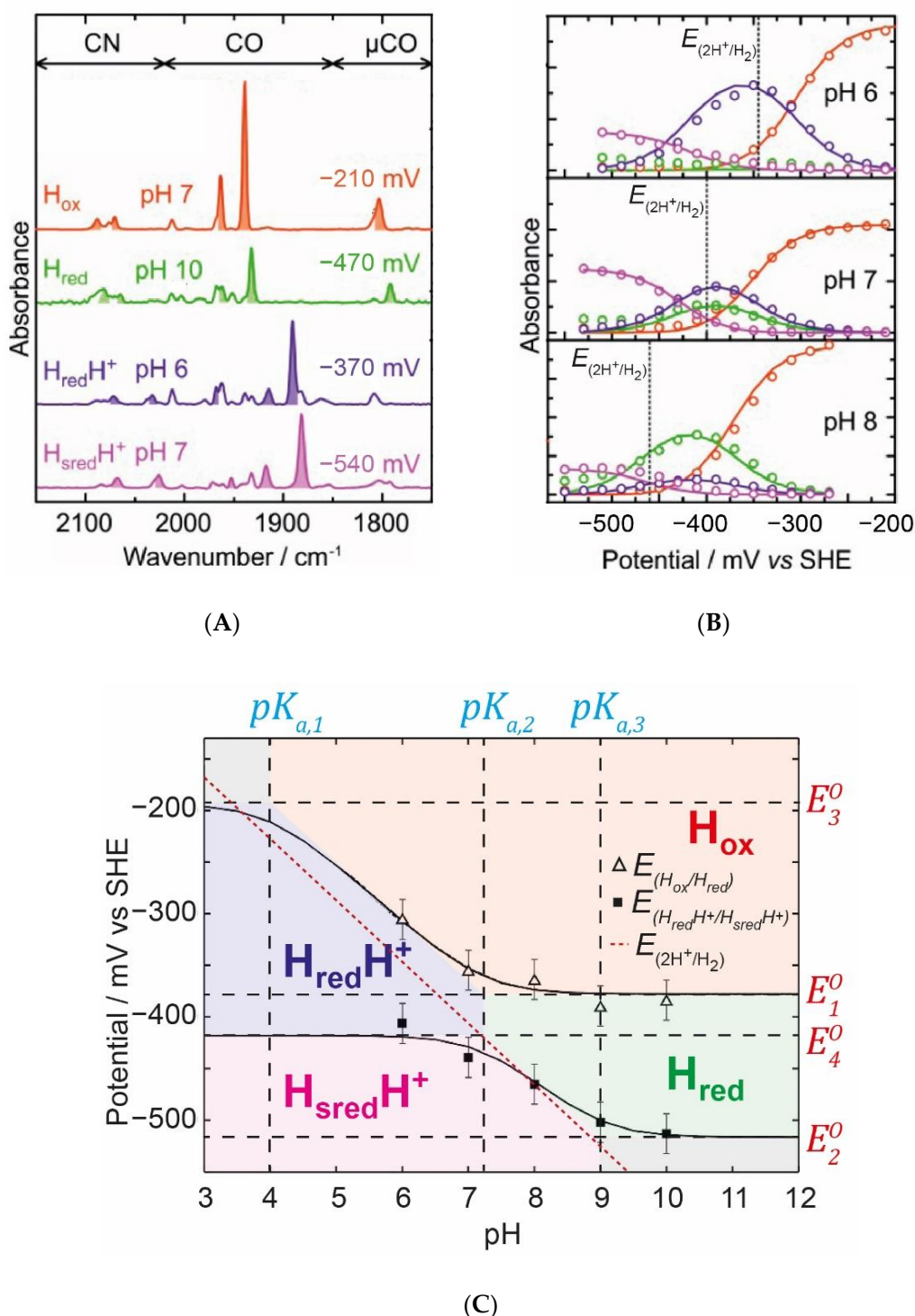
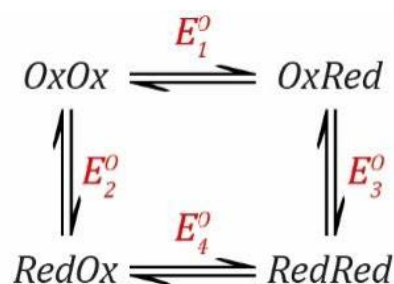


Figure 10. Application of the simple model for [FeFe] hydrogenase to experimental IR spectro-electrochemical data. **(A)** IR spectra recorded at various pH values and applied potentials, measured at 288 K. **(B)** Reductive titrations obtained from the IR spectro-electrochemical data. The dotted black lines represent the thermodynamic potential for the $2H^+/H_2$ couple at each pH. **(C)** The Pourbaix diagram showing the regions with respect to pH and applied potential (E) where each of the four states (H_{ox} , H_{red} , $H_{red}H^+$, and $H_{sred}H^+$) dominates. The grey areas in the top left and bottom right corners represent the areas where the $H_{ox}H^+$ and H_{sred} species are expected to be observed. However, these have not yet been seen experimentally. The thermodynamic potential of the $2H^+/H_2$ couple is plotted vs. pH (red dotted line) for comparison. Adapted with permission from [35]. Copyright 2017 American Chemical Society.

Effectively, the enzyme is optimised so that the potentials of the $Ox(H)/Red(H)$ and $Red(H)/Sred(H)$ are as close as possible to the thermodynamic $2H^+/H_2$ potential. This can be seen again in the Pourbaix diagram (Figure 9F for the model and Figure 10C for the model applied to CrHydA1). The thermodynamic $2H^+/H_2$ potential is shown as a dotted line. It is clear that, at a neutral pH, both transitions ($Ox(H)/Red(H)$ and $Red(H)/Sred(H)$) are close to the thermodynamic $2H^+/H_2$ potential. In Figure 10C, the midpoint potential of the H_{ox}/H_{red} and H_{red}/H_{sred} transitions are plotted against the pH and are fitted with curves based on the model described above, with areas coloured to indicate where the various states dominate (in analogy to Figure 9F). Ideally, both curves would fit perfectly to the $2H^+/H_2$ potential at all pH values. However, using this model, it is not possible to generate such curves. One expects, therefore, at extreme pH values, to start to observe deviations of the catalytic efficiency in one direction. At a low pH, we expect a slight overpotential from H^+ reduction, while, at a high pH, we expect a slight overpotential for H_2 oxidation. This seems to fit well with the known behaviour of the [FeFe] hydrogenase from CrHydA1 in IR spectro-electro-chemical titrations [33,35,44,45], but, interestingly, not with those from more complex enzymes including accessory iron-sulfur clusters [32,34]. In order to understand the behaviour in these more complex enzymes, we first need to deal with the concept of redox anti-cooperativity.

2.4. Redox Anticooperativity Model

In Section 2.2, we dealt with what happens when we can oxidise/reduce and protonate/deprotonate simultaneously, but we could also have two simultaneous oxidation/reduction events. Such a situation could be used to describe two iron-sulfur clusters located close to one another. These two redox events may be independent (i.e., their redox potentials do not influence one another) or they may be dependent (i.e., their redox potentials influence one another) [46]. This influence can be positive or negative. If reduction of one cluster makes it easier to reduce the second cluster, this would give us redox cooperativity. If reduction of one cluster makes it more difficult to reduce the second cluster, this would give us redox anti-cooperativity. Scheme 5 shows a simple model.



Scheme 5. Scheme showing the reactions in a simple two-step redox model. The doubly oxidised species $OxOx$ can be reduced to $OxRed$ with a redox potential of E_1^0 or to $RedOx$ with a redox potential of E_2^0 . $OxRed$ and $RedOx$ can then be further reduced to $RedRed$ with redox potentials of E_3^0 and E_4^0 , respectively.

This situation is somewhat similar to the PCET scenario described in Section 2.2 except that it involves two electrons rather than one electron and one proton. All steps are redox steps and defined by the Nernst equation.

$$E = E_1^0 - \frac{RT}{nF} \ln \left(\frac{[OxRed]}{[OxOx]} \right)$$

$$E = E_2^0 - \frac{RT}{nF} \ln \left(\frac{[RedOx]}{[OxOx]} \right)$$

$$E = E_3^0 - \frac{RT}{nF} \ln \left(\frac{[RedRed]}{[OxRed]} \right)$$

$$E = E_4^O - \frac{RT}{nF} \ln \left(\frac{[RedRed]}{[RedOx]} \right)$$

These equations can be rearranged to get everything in terms of $[OxOx]$ (see SI Section S2 for a complete derivation).

$$[OxOx] = \frac{1}{1 + \alpha(1 + \gamma) + \beta} \quad (29)$$

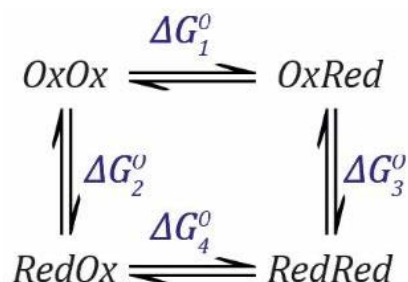
where:

$$\alpha = \exp \frac{nF}{RT} (E_1^O - E) \quad (30)$$

$$\beta = \exp \frac{nF}{RT} (E_2^O - E) \quad (31)$$

$$\gamma = \exp \frac{nF}{RT} (E_3^O - E) \quad (32)$$

As before, in order to arrive at this result, we only need to consider the three reduction events defined by E_1^O , E_2^O , and E_3^O . E_4^O can be calculated considering the thermodynamic square (Scheme 6) as follows.



Scheme 6. Scheme showing the free energies associated with reactions in a simple two-step redox model. The doubly oxidised species $OxOx$ can be reduced to $OxRed$ or $RedOx$ with free energy changes ΔG_1 and ΔG_2 , respectively. $OxRed$ and $RedOx$ can then be further reduced to $RedRed$ with free energy changes ΔG_3 and ΔG_4 , respectively.

The rules still apply so that the free energy change is the same regardless which pathway is taken. Thus, going from $OxOx$ to $RedRed$ via $OxRed$ or via $RedOx$ have the same overall free energy change. Therefore, we can define the following equation.

$$\Delta G_1^O + \Delta G_3^O = \Delta G_2^O + \Delta G_4^O \quad (33)$$

where:

$$\Delta G_1^O = -nFE_1^O$$

$$\Delta G_2^O = -nFE_2^O$$

$$\Delta G_3^O = -nFE_3^O$$

$$\Delta G_4^O = -nFE_4^O$$

These equations can then be substituted into Equation (33) and rearranged to give E_4^O .

$$\begin{aligned} -nFE_1^O + (-nFE_3^O) &= -nFE_2^O + (-nFE_4^O) \\ nFE_1^O + nFE_3^O &= nFE_2^O + nFE_4^O \\ nFE_4^O &= nFE_1^O - nFE_2^O + nFE_3^O \\ E_4^O &= E_1^O - E_2^O + E_3^O \end{aligned} \quad (34)$$

Now, we can set up two different situations, one in which we have two independent redox events (i.e., $E_1^O = E_4^O$ and $E_2^O = E_3^O$) and one in which the redox events are dependent (i.e., $E_1^O \neq E_4^O$ and $E_2^O \neq E_3^O$). In Figure 11, the independent situation is shown where $E_1^O = E_4^O = -390$ mV and $E_2^O = E_3^O = -410$ mV (the average E^O is -400 mV).

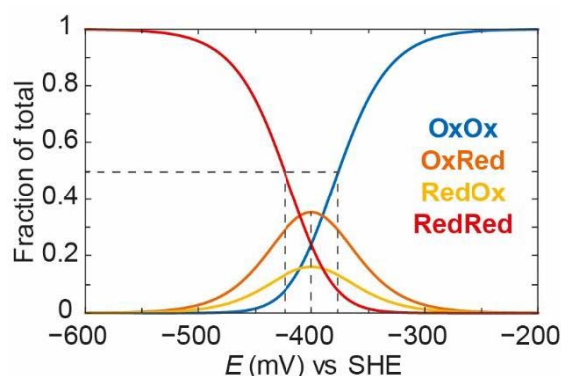


Figure 11. Variation of the fraction (out of 1) of the oxidised (OxOx, blue), partially reduced (OxRed, dark orange, RedOx, light orange) and fully reduced (RedRed, red) species as a function of the applied potential. The curves were obtained using Equations (29)–(32), with $E_1^O = E_4^O = -390$ mV and $E_2^O = E_3^O = -410$ mV (i.e., no redox anti-cooperativity), giving an average E^O of -400 mV, for comparison with earlier figures.

It can be seen that, as the potential goes from positive to negative, OxOx decreases and both OxRed and RedOx increase. One can think of this as a single electron entering the enzyme and equilibrating between both clusters depending on their intrinsic redox potentials. In this case, OxRed is more dominant because it has a more positive redox potential (-390 mV vs. -410 mV). It should also be noted that the decrease in the OxOx state follows a titration with an “apparent” midpoint potential more positive than -390 mV. In fact, the “apparent” midpoint potential is -380 mV. This is because both the OxOx/OxRed and OxOx/RedOx couples are titrating at the same time. This means that the OxOx species is lost at slightly more positive potentials than the values of E_1^O and E_2^O . The take-home message here is that these systems often behave in ways that, at first glance, seem non-intuitive, and it is only by studying the models that it is possible to fully understand their behaviour. As the second electron enters the enzyme, it will equilibrate among the remaining oxidised clusters and both OxRed and RedOx start to decrease as RedRed increases. RedRed increases with an “apparent” midpoint potential of -420 mV, which is slightly more negative than the values of E_3^O and E_4^O .

Next, we can apply the same model but introduce some redox anti-cooperativity. In Figure 12, we have defined $E_4^O = E_1^O - 100$ mV, i.e., there is 100 mV of redox anti-cooperativity, or the redox potential of one cluster is 100 mV more negative when the other cluster is reduced. Because of the thermodynamic square, this also means that $E_3^O = E_2^O - 100$ mV, and the redox potential of the second cluster is also 100 mV more negative when the other cluster is reduced. We have redefined the intrinsic redox potentials $E_1^O = -340$ mV and $E_2^O = -360$ mV so that the average E^O is still -400 mV, as in Figure 11.

As can be observed, OxOx decreases with a very positive “apparent” midpoint potential (-330 mV). OxRed and RedOx increase to a much greater extent and persist for longer until the RedRed state starts to increase with an “apparent” midpoint potential of -470 mV. These “apparent” midpoint potentials are 50 mV more positive and more negative, respectively, than those observed in Figure 11, reflecting the 100 mV redox anti-cooperativity.

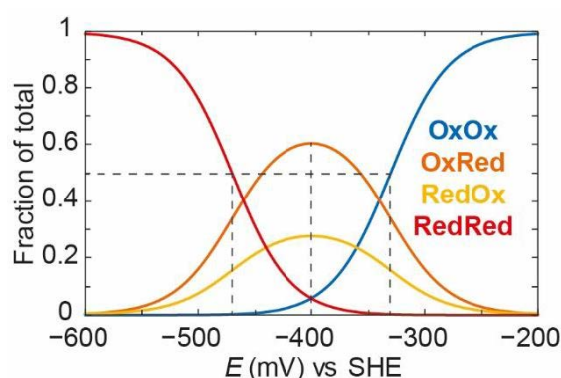
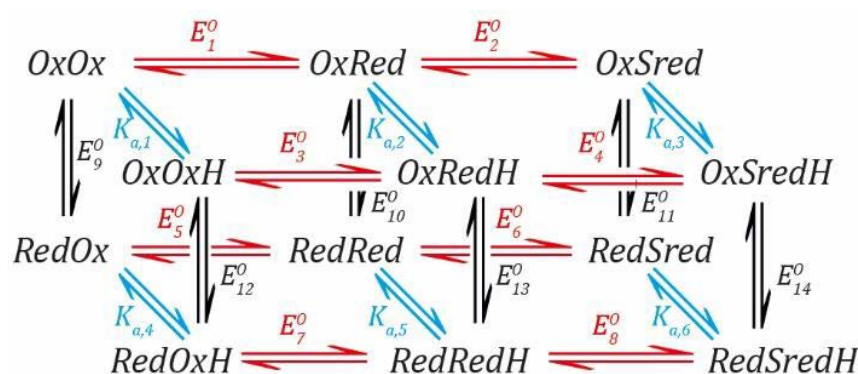


Figure 12. Variation of the fraction (out of 1) of the oxidised (*OxOx*, blue), partially reduced (*OxRed*, dark orange, *RedOx*, light orange) and fully reduced (*RedRed*, red) species as a function of the applied potential. The curves were obtained using Equations (29)–(32), with $E_1^O = -340$ mV, $E_2^O = -360$ mV, $E_3^O = -460$ mV, $E_4^O = -440$ mV (i.e., 100 mV of redox anti-cooperativity), giving an average E^O of -400 mV, for a comparison with Figure 11.

This model was used to fit IR spectro-electrochemistry data from the [FeFe] hydrogenase from *Desulfovibrio desulfuricans* (*DdHydAB*) [34]. For the sake of brevity, we have not reproduced the fitting of the experimental data in this review. However, the interested reader is highly recommended to read Reference [34], where the simple anti-cooperativity model was applied to *DdHydAB* with PDT in the [2Fe] cluster. This enzyme possesses the active site H-cluster as well as two accessory iron-sulfur clusters (F-clusters). Unusual behaviour was observed in IR spectro-electrochemical redox titrations of this enzyme in which the active site had been artificially matured with a diiron cluster containing PDT. Since PDT cannot be protonated at the bridgehead atom, reduction only occurs at the [4Fe-4S]_H subcluster of the H-cluster giving small (5–10 cm⁻¹) shifts in the CO and CN⁻ bands to lower energy. These titrations showed non-Nernstian behaviour that indicated reduction of the proximal F-cluster caused the redox potential of the [4Fe-4S]_H to become more negative. In fact, the reduction of the proximal F-cluster could be observed directly as minute (<2 cm⁻¹) shifts in the IR bands of both the H_{ox} and H_{red} states. These data were fitted using the redox anti-cooperativity model described above and yielded a value of 118 mV for the interaction between the two clusters. This demonstrates that the modelling approach described in this case is not only illustrative but also practically useful for understanding spectro-electrochemical data and studying enzyme mechanisms. Since the PDT cofactor cannot be protonated, this simplified the number of redox states observed, and allowed the redox anti-cooperativity model to be investigated. However, to fully understand the behaviour of the natural H-cluster containing ADT in an F-cluster containing [FeFe] hydrogenase, it is necessary to incorporate redox anti-cooperativity into the full H-cluster model described in Section 2.3. In the next section, this is exactly what we will do.

2.5. Redox Anticooperativity Model for the Active [FeFe] Hydrogenase

In Section 2.1, we laid the foundations, showing the behaviour of a simple one electron redox and (de)protonation events. In Section 2.2, we combined redox and (de)protonation into a proton-coupled electron transfer model. Then, in Section 2.3, we added a second redox step to build a simple model that can be used to describe thermodynamic titrations of the H-cluster in the F-cluster free [FeFe] hydrogenase *CrHydA1*. In Section 2.4, we took a detour to look at what happens when two redox events occur adjacent to one another and can influence each other by redox anti-cooperativity. Now, we will combine what we have learned to build up a highly complex model containing both PCET and redox anti-cooperativity. Each species can now exist in three redox states of the H-cluster (*Ox*, *Red*, and *Sred*), two protonation states, and also two different redox states of the proximal F-cluster, making the model “three-dimensional” (Scheme 7).



Scheme 7. Model for active [FeFe] hydrogenase including redox anti-cooperativity. The steps and redox potentials indicated in *Red* are the reduction of the H-cluster first from *Ox* to *Red*, then *Red* to *Sred*. The steps and K_a values indicated in blue are protonation of the H-cluster in the *Ox*, *Red*, and *Sred* states. The steps and redox potentials indicated in black are the reduction of the proximal F-cluster from *Ox* to *Red*.

As before, each E^O value defines the Nernst relationship between a reduced and an oxidised species and each K_a value defines the relationship between a protonated and a deprotonated species. Once all the equations are described for each pathway, they can all be rearranged to get everything in terms of $[OxOx]$ (for the full derivation, please refer to the Supplementary Materials Section S3). Here, we will simply present the final equation for $[OxOx]$ in terms of E^O values and K_a values, in all its complexity.

$$[OxOx] = \frac{1}{1 + \alpha_1(1 + \alpha_2) + 10^{(pK_{a,1} - pH)} \{1 + \alpha_3(1 + \alpha_4)\} + \alpha_9(1 + \alpha_5(1 + \alpha_6) + 10^{(pK_{a,4} - pH)} \{1 + \alpha_7(1 + \alpha_8)\})} \quad (35)$$

where $\alpha_n = \exp \frac{nF}{RT} (E_n^O - E)$

As with the previous models, it was only necessary to use a limited number of the parameters. The rest can be calculated by considering the thermodynamic cycles. We used E_1^O to E_9^O as well as $K_{a,1}$ and $K_{a,4}$. Therefore, we need to calculate E_{10}^O to E_{14}^O as well as $K_{a,2}$, $K_{a,3}$, $K_{a,5}$, and $K_{a,6}$ (see SI Section S3 for derivations of the equations).

$$E_{10}^O = E_5^O - E_1^O + E_9^O \quad (36)$$

$$E_{11}^O = E_6^O - E_2^O + E_{10}^O \quad (37)$$

$$E_{12}^O = E_9^O + \frac{RT}{nF} \ln \frac{K_{a,1}}{K_{a,4}} \quad (38)$$

$$E_{13}^O = E_7^O - E_3^O + E_{12}^O \quad (39)$$

$$E_{14}^O = E_8^O - E_4^O + E_{13}^O \quad (40)$$

$$K_{a,2} = K_{a,1} \exp \left[\frac{nF}{RT} (E_1^O - E_3^O) \right] \quad (41)$$

$$K_{a,3} = K_{a,2} \exp \left[\frac{nF}{RT} (E_2^O - E_4^O) \right] \quad (42)$$

$$K_{a,5} = K_{a,4} \exp \left[\frac{nF}{RT} (E_5^O - E_7^O) \right] \quad (43)$$

$$K_{a,6} = K_{a,5} \exp \left[\frac{nF}{RT} (E_6^O - E_8^O) \right] \quad (44)$$

Now these equations can be used to plot how the concentrations of intermediates vary with the applied potential as we did before for the simpler situation. In Figure 13, the same

parameters have been used as for Figure 9A to describe the situation when the proximal F-cluster is oxidised. Then redox anti-cooperativity is added, such that *RedOx/RedRed* and *RedRedH/RedSredH* transitions are 100 mV more negative than the *OxOx/OxRed* and *OxRedH/OxSredH* transitions, respectively (affecting the steps that involve reduction of the proximal F-cluster and $[4\text{Fe-4S}]_{\text{H}}$). The intrinsic redox potential of the proximal F-cluster was set to -370 mV (i.e., the *OxOx/RedOx* transition has a redox potential of -370 mV). For Figure 13, it has been assumed that states in which the proximal F-cluster is reduced cannot be spectroscopically distinguished from those in which the F-cluster is oxidised so that their populations are added together, i.e., $[\text{Ox}] = [\text{OxOx}] + [\text{RedOx}]$, etc. Lastly, states with essentially zero population across the potential range are not shown.

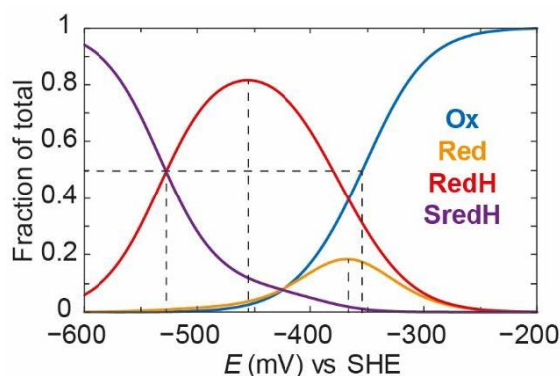


Figure 13. Variation of the fraction (out of 1) of the deprotonated oxidised (*Ox*, blue), deprotonated reduced (*Red*, orange), protonated reduced (*RedH*, red), and protonated super-reduced (*SredH*, purple) species as a function of the applied potential at pH 7. The curves were obtained using Equation (35) (α_n values defined in SI Section S3), with $E_1^O = -370$ mV, $E_2^O = -700$ mV, $E_3^O = -100$ mV, and $E_4^O = -430$ mV giving an average E^O of -400 mV, for a comparison with earlier figures, redox anti-cooperativity of 100 mV resulting in $E_5^O = -470$ mV, $E_6^O = -700$ mV, $E_7^O = -100$ mV, and $E_8^O = -530$ mV, $E_9^O = -370$ mV, $K_{a,1} = 3.16 \times 10^{-3}$ ($pK_{a,1} = 2.5$), and $K_{a,4} = 3.16 \times 10^{-3}$ ($pK_{a,4} = 2.5$). The calculated parameters (using Equations (36)–(44)) were then: $E_{10}^O = -470$ mV, $E_{11}^O = -470$ mV, $E_{12}^O = -370$ mV, $E_{13}^O = -370$ mV, and $E_{14}^O = -470$ mV, $K_{a,2} = 8.58 \times 10^{-8}$ ($pK_{a,2} = 7.1$), $K_{a,3} = 2.33 \times 10^{-12}$ ($pK_{a,3} = 11.6$), $K_{a,5} = 1.75 \times 10^{-9}$ ($pK_{a,5} = 8.6$), $K_{a,6} = 2.33 \times 10^{-12}$ ($pK_{a,6} = 11.6$). $\text{Ox} = \text{OxOx} + \text{RedOx}$, $\text{Red} = \text{OxRed} + \text{RedRed}$, $\text{RedH} = \text{OxRedH} + \text{RedRedH}$, $\text{SredH} = \text{OxSredH} + \text{RedSredH}$. *OxH* and *Sred* are not shown because their concentrations are effectively zero.

From Figure 13, it can be seen that, as the applied potential becomes more negative, the *Ox* state disappears and is replaced by a mixture of *Red* and *RedH*. However, as the potential becomes even more negative, *Red* decreases while *RedH* increases further. At the most negative potentials, *RedH* also decreases and *SredH* appears. This behaviour almost exactly reproduces the observations made during IR spectro-electrochemical titrations of *DdHydAB* matured with the ADT-containing cofactor [34]. At first, this behaviour seemed entirely inexplicable. However, consideration of redox anti-cooperativity, which is clearly observed in the case of the PDT variant, allowed this behaviour to be understood. As the potential decreases, an electron enters the enzyme and equilibrates between the clusters, giving a mixture of *RedOx* (F-cluster reduced), *OxRed* ($[4\text{Fe-4S}]_{\text{H}}$ subcluster reduced), and *OxRedH* ($[2\text{Fe}]_{\text{H}}$ subcluster reduced and protonated). As the applied potential becomes even more negative, a second electron enters the enzyme and fills the empty spaces, i.e., *RedOx* and *OxRed* are converted to *RedRed*, and *OxRedH* is converted to *RedRedH* and a small amount of *OxSredH*. However, *RedRed* is very unstable due to redox anti-cooperativity between the proximal F-cluster and the $[4\text{Fe-4S}]_{\text{H}}$ subcluster, and prefers to make *RedRedH* by protonation of the $[2\text{Fe}]_{\text{H}}$ subcluster followed by an electronic rearrangement. Thus, at more negative potentials, *RedRedH* accumulates. Now the question is: why is *RedRedH* more stable than *OxSredH*? This is likely because formation of the *SredH* state requires a large amount of electron density on the H-cluster, while *RedRedH* allows the two electrons to

be stored on separate cofactors, one on the H-cluster and a second on the proximal F-cluster. Effectively though, the *RedRedH* state in *DdHydAB* has the same ability to produce H_2 as the *SredH* state in *CrHydA1* (both have two electrons and one proton). However, *RedRedH* can be formed at more positive potentials than *SredH*, allowing H^+ reduction to start even closer to the thermodynamic $2H^+/H_2$ potential. Likewise, the *Ox* state is formed at slightly more negative potentials than in *CrHydA1*, allowing H_2 oxidation to start even closer to the thermodynamic $2H^+/H_2$ potential. Overall, this behaviour of the F-cluster containing [FeFe] hydrogenases may help to explain their excellent efficiency and reversibility for $2H^+/H_2$ interconversion when compared with the F-cluster free *CrHydA1* [44,47].

Although we hypothesise that redox anti-cooperativity is purely an electrostatic effect from repulsion of electrons on the two reduced clusters, the factors governing this behaviour remain unclear. Furthermore, in addition to the effects described above, redox anti-cooperativity may also be involved in determining the catalytic bias of [FeFe] hydrogenases (i.e., whether the enzyme favours H_2 oxidation or H^+ reduction). It should be noted, however, that the factors determining catalytic bias are complex and include interactions between the active site and the protein matrix, which are essential for stabilising the various states of the H-cluster [48]. Deletion of the F-cluster domain in a number of [FeFe] hydrogenases has a direct influence on the catalytic bias, possibly supporting a role for redox anti-cooperativity [49,50].

It should be noted that, in this model, as well as the previous model from Section 2.4, we have only considered the interaction between the proximal F-cluster and the $[4Fe-4S]_H$ sub-cluster. In *DdHydAB*, a distal F-cluster is also present. However, the spectro-electrochemical titrations of this enzyme could be well reproduced without considering this cluster. This could indicate that the potential of this cluster is very positive in relation to the proximal F-cluster, and so it is essentially in the reduced state throughout the titrations, or that the redox anti-cooperativity between the distal and proximal F-clusters, and between the distal F-cluster and the H-cluster, is negligible. In a recent study of the F-cluster containing [FeFe] hydrogenase from *Clostridium pasteurianum* (*CpHydA1*), it was necessary to include a second redox anti-cooperative interaction into the model [51]. In this case, the second cluster appears to have a more negative redox potential than the proximal cluster.

3. Discussion

In this review, we have outlined how some simple and some more complex thermodynamic models can be built up from basic principles and how they can be applied to study the behaviour of [FeFe] hydrogenases. One can imagine even more complicated models, including redox anti-cooperativity from the multiple F-clusters in highly complex enzymes such as *CpHydA1*, or including additional catalytic intermediates, such as H_{hyd} . Additional protonation sites have been suggested on the $[4Fe-4S]_H$ subcluster. These could also be incorporated into such models. Lastly, ligand binding such as CO, which is a potent inhibitor of [FeFe] hydrogenases, or formation of inactive states, such as H_{inact} by binding of H_2S , could be modelled using this approach. Development of such models does not require anything more complicated than what was laid out in the current manuscript. However, a difficult issue to overcome in such large and complex models is the complexity and redundancy in fitting the models to experimental data. Already for simple models of the H-cluster, a range of potential fits can be found given the limited experimental data ([FeFe] hydrogenases tend to be unstable outside of the pH 5 to 10 range). Furthermore, under extreme experimental conditions, additional side-reactions may be observed that cannot be easily accommodated by simple models. In any case, the simple models described in this review have already been proven sufficiently descriptive for a range of enzymes under conditions close to those observed physiologically, and may prove useful in the future for researchers in the [FeFe] hydrogenase field.

There is no good reason why the same models cannot be applied to other enzymes. We have tried in this review to make our models as generalised as possible using *Ox*, *OxH*, *Red*, *RedH*, etc. Since the principles of thermodynamics are universal, so too are the models

based on these principles. The mechanism of the [NiFe] hydrogenase is still not completely understood [3]. However, similar pH dependent spectro-electrochemical experiments together with modelling may shed further light on this. [NiFe] hydrogenase is known to cycle between Ni-Si_A, Ni-C, Ni-L, and Ni-R states. Ni-Si_A is the most oxidised state, while Ni-L and Ni-C are both one electron reduced and protonated. Ni-R is two electrons reduced and singly protonated. Then, with respect to the models described in this review, Ni-Si_A can be modelled as *Ox*, while Ni-L and Ni-C can be represented as two conformations of *RedH* and Ni-R can be modelled as *SredH*. In principle, the *OxH*, *Red*, and *Sred* states can also be modelled, but due to the specific *pK_a* values and potentials, these states are not accumulated experimentally. Modelling the behaviour of the [NiFe] hydrogenase and comparing with [FeFe] hydrogenase may shed light on why these enzymes are generally biased for H₂ oxidation rather than H⁺ reduction, and possibly help us to understand how active site changes, such as amino acid substitutions, affect enzyme activity and spectroscopic properties.

One can also imagine how similar models can be constructed and used to study more complex enzymes such as the Ni-dependent carbon monoxide dehydrogenase (CODH) and MoFe nitrogenase among others. Models for CODH should, in principle, be quite similar to those for hydrogenase as both enzymes require 2e⁻ and 2H⁺. This enzyme is known to cycle between C_{red1}, C_{red2}, and C_{int} states [52], and may or may not involve formation of hydrides [53]. C_{red1} can be modelled with *Ox*, C_{int} with either *Red* or *RedH*, and C_{red2} with either *Sred* or *SredH*. In this case, there are no useful IR bands available for characterising the oxidation/protonation states of the active site. This enzyme reacts with CO and CO₂, and binds CN⁻ as an inhibitor. These ligands could potentially be used to characterise the behaviour of the C-cluster via IR spectroscopy as is done for hydrogenases. Electron paramagnetic resonance (EPR) or UV-vis spectro-electrochemical titrations can also be used. However, these are complicated by the additional iron-sulfur clusters. In the [FeFe] hydrogenase field, it is lucky that enzymes containing only the active site, such as CrHydA1, can be studied. Recently, forms of the [NiFe] hydrogenase lacking the accessory FeS clusters have been reported [54], allowing the active site to be studied independently of the accessory clusters.

Finally, a highly desirable target of study is the nitrogenase, capable of reducing N₂ to two molecules of NH₃ and at least one molecule of H₂ using at least 8H⁺ and 8e⁻, as well as at least 16 molecules of ATP [55,56]. The mechanism of this enzyme is thought to be highly complex involving multiple proton coupled electron transfer steps as well as formation of hydride intermediates and release of an obligatory H₂ molecule upon N₂ binding, which is followed by formation of some kind of nitrogen-bound intermediates on the pathway to form ammonia. The prospect of studying such an enzyme using thermodynamic titrations is daunting, especially considering that electrons have to be pumped in using a complex mechanism involving ATP hydrolysis and a deficit spending model for electron transfer from the accessory P-cluster [57]. However, even here, simple thermodynamic models may be of use for describing the electron and proton distribution under certain conditions. For example, in the E₁ state, the FeMo cofactor is thought to have acquired one electron and one proton. This can then be modelled as *RedH* while the E₀ state can be modelled by *Ox*. By carefully studying the behaviour of E₁ and E₀ over a wide pH range, it may be possible to learn about the factors involved in PCET. Potentially, similar studies could be applied to each of the E_n states, helping to understand the driving forces involved in the formation of hydride states and ligand binding. While it may not be possible to apply the same exact models described here for studying [FeFe] hydrogenases, we are certain that building a thermodynamic picture of events in nitrogenases and other complex metalloenzymes will contribute to our understanding of their mechanism.

4. Conclusions

In this review, we have tried to provide a foundation in building thermodynamic models and we have reviewed how this model has been applied to experimental data to

extract important thermodynamic parameters, hopefully dispelling the notion that these are somehow overly complex and inaccessible. We hope this review is of use to those in the field of metalloenzymes. In the [FeFe] hydrogenase field, the use of these modelling techniques have been crucial in providing a basis for understanding surprising observations made during experiments grasping complex phenomena, e.g., redox anti-cooperativity. Moreover, developing and applying models provides an accessible way of learning about how basic concepts can lead to complicated behaviour, ultimately helping to understand the fascinating world we live in.

Supplementary Materials: The following are available online at <https://www.mdpi.com/2073-4344/11/2/238/s1>. Section S1—Derivation of equations for a simple model for the [FeFe] hydrogenase. Section S2—Derivation of equations for a redox anti-cooperativity model. Section S3—Derivation of equations for a redox anti-cooperativity model for the active [FeFe] hydrogenase. Models.xlsx.

Author Contributions: J.A.B., P.R.-M., and A.H.-B. contributed equally to the writing of this manuscript. All authors have read and agreed to the published version of the manuscript.

Funding: This research was funded by the Max Planck Society (J.A.B.) and the Deutsche Forschungsgemeinschaft (DFG) SPP1927 “Iron-Sulfur for Life: Cooperative function of Iron-Sulfur Centers in Assembly, Biosynthesis, Catalysis, and Disease”, Project BI 2198/1-1 (J.A.B.). P.R.-M. is supported financially by the European Research Council (ERC-2018-CoG BiocatSusChem 819580, to K.A. Vincent), and acknowledges Linacre College Oxford for her Junior Research Fellowship.

Data Availability Statement: No new data were created or analyzed in this study. Data sharing is not applicable to this article.

Conflicts of Interest: The authors declare no conflict of interest.

References

1. Armaroli, N.; Balzani, V. The hydrogen issue. *ChemSusChem* **2011**, *4*, 21–36. [CrossRef] [PubMed]
2. Rodríguez-Maciá, P.; Dutta, A.; Lubitz, W.; Shaw, W.J.; Rüdiger, O. Direct comparison of the performance of a bio-inspired synthetic nickel catalyst and a [NiFe]-hydrogenase, both covalently attached to electrodes. *Angew. Chem. Int. Ed.* **2015**, *54*, 12303–12307. [CrossRef]
3. Lubitz, W.; Ogata, H.; Rüdiger, O.; Reijerse, E. Hydrogenases. *Chem. Rev.* **2014**, *114*, 4081–4148. [CrossRef]
4. Laureanti, J.A.; O’Hagan, M.; Shaw, W.J. Chicken fat for catalysis: A scaffold is as important for molecular complexes for energy transformations as it is for enzymes in catalytic function. *Sustain. Energy Fuels* **2019**, *3*, 3260–3278. [CrossRef]
5. Land, H.; Senger, M.; Berggren, G.; Stripp, S.T. Current State of [FeFe]-hydrogenase research—biodiversity and spectroscopic investigations. *ACS Catal.* **2020**, *10*, 7069–7086. [CrossRef]
6. Wittkamp, F.; Senger, M.; Stripp, S.T.; Apfel, U.P. [FeFe]-hydrogenases: Recent developments and future perspectives. *Chem. Commun.* **2018**, *54*, 5934–5942. [CrossRef]
7. Völler, J.-S. Air-stable [FeFe] hydrogenases. *Nat. Catal.* **2018**, *1*, 564. [CrossRef]
8. Goldet, G.; Brandmayr, C.; Stripp, S.T.; Happe, T.; Cavazza, C.; Fontecilla-Camps, J.C.; Armstrong, F.A. Electrochemical kinetic investigations of the reactions of [FeFe]-hydrogenases with carbon monoxide and oxygen: Comparing the importance of gas tunnels and active-site electronic/redox effects. *J. Am. Chem. Soc.* **2009**, *131*, 14979–14989. [CrossRef]
9. Stripp, S.T.; Goldet, G.; Brandmayr, C.; Sanganas, O.; Vincent, K.A.; Haumann, M.; Armstrong, F.A.; Happe, T. How oxygen attacks [FeFe] hydrogenases from photosynthetic organisms. *Proc. Natl. Acad. Sci. USA* **2009**, *106*, 17331–17336. [CrossRef]
10. Kubas, A.; Orain, C.; De Sancho, D.; Saujet, L.; Sensi, M.; Gauquelin, C.; Meynial-Salles, I.; Soucaille, P.; Bottin, H.; Baffert, C.; et al. Mechanism of O₂ diffusion and reduction in FeFe hydrogenases. *Nat. Chem.* **2017**, *9*, 88–95. [CrossRef]
11. Rodríguez-Maciá, P.; Reijerse, E.J.; van Gastel, M.; DeBeer, S.; Lubitz, W.; Rüdiger, O.; Birrell, J.A. Sulfide protects [FeFe] hydrogenases from O₂. *J. Am. Chem. Soc.* **2018**, *140*, 9346–9350. [CrossRef]
12. Rodríguez-Maciá, P.; Galle, L.M.; Bjornsson, R.; Lorent, C.; Zebger, I.; Yoda, Y.; Cramer, S.P.; DeBeer, S.; Span, I.; Birrell, J.A. Caught in the H_{inact}: Crystal structure and spectroscopy reveal a sulfur bound to the active Site of an O₂-stable state of [FeFe] hydrogenase. *Angew. Chem. Int. Ed.* **2020**, *59*, 16786–16794. [CrossRef]
13. Oughli, A.A.; Conzuelo, F.; Winkler, M.; Happe, T.; Lubitz, W.; Schuhmann, W.; Rüdiger, O.; Plumeré, N. A redox hydrogel protects the O₂-sensitive [FeFe]-hydrogenase from *Chlamydomonas reinhardtii* from oxidative damage. *Angew. Chem. Int. Ed.* **2015**, *54*, 12329–12333. [CrossRef]
14. Oughli, A.A.; Hardt, S.; Rüdiger, O.; Birrell, J.A.; Plumeré, N. Reactivation of sulfide-protected [FeFe] hydrogenase in a redox-active hydrogel. *Chem. Commun.* **2020**, *56*, 9958–9961. [CrossRef]
15. Morra, S.; Arizzi, M.; Valetti, F.; Gilardi, G. Oxygen Stability in the new [FeFe]-hydrogenase from *Clostridium beijerinckii* SM10 (CbA5H). *Biochemistry* **2016**, *55*, 5897–5900. [CrossRef]

16. Corrigan, P.S.; Tirsch, J.L.; Silakov, A. Investigation of the unusual ability of the [FeFe] hydrogenase from *Clostridium beijerinckii* to access an O₂-protected state. *J. Am. Chem. Soc.* **2020**, *142*, 12409–12419. [[CrossRef](#)] [[PubMed](#)]
17. Nicolet, Y.; Piras, C.; Legrand, P.; Hatchikian, C.E.; Fontecilla-Camps, J.C. *Desulfovibrio desulfuricans* iron hydrogenase: The structure shows unusual coordination to an active site Fe binuclear center. *Structure* **1999**, *7*, 13–23. [[CrossRef](#)]
18. Peters, J.W.; Lanzilotta, W.N.; Lemon, B.J.; Seefeldt, L.C. X-ray crystal structure of the Fe-only hydrogenase (CpI) from *Clostridium pasteurianum* to 1.8 angstrom resolution. *Science* **1998**, *282*, 1853–1858. [[CrossRef](#)] [[PubMed](#)]
19. Silakov, A.; Wenk, B.; Reijerse, E.; Lubitz, W. ¹⁴N HYSCORE investigation of the H-cluster of [FeFe] hydrogenase: Evidence for a nitrogen in the dithiol bridge. *Phys. Chem. Chem. Phys.* **2009**, *11*, 6592–6599. [[CrossRef](#)] [[PubMed](#)]
20. Mulder, D.W.; Guo, Y.; Ratzloff, M.W.; King, P.W. Identification of a catalytic iron-hydride at the H-cluster of [FeFe]-hydrogenase. *J. Am. Chem. Soc.* **2017**, *139*, 83–86. [[CrossRef](#)]
21. Mulder, D.W.; Ratzloff, M.W.; Bruschi, M.; Greco, C.; Koonce, E.; Peters, J.W.; King, P.W. Investigations on the role of proton-coupled electron transfer in hydrogen activation by [FeFe]-hydrogenase. *J. Am. Chem. Soc.* **2014**, *136*, 15394–15402. [[CrossRef](#)]
22. Reijerse, E.J.; Pham, C.C.; Pelmenschikov, V.; Gilbert-Wilson, R.; Adamska-Venkatesh, A.; Siebel, J.F.; Gee, L.B.; Yoda, Y.; Tamasaku, K.; Lubitz, W.; et al. Direct observation of an iron-bound terminal hydride in [FeFe]-hydrogenase by nuclear resonance vibrational spectroscopy. *J. Am. Chem. Soc.* **2017**, *139*, 4306–4309. [[CrossRef](#)]
23. Winkler, M.; Senger, M.; Duan, J.; Esselborn, J.; Wittkamp, F.; Hofmann, E.; Apfel, U.P.; Stripp, S.T.; Happe, T. Accumulating the hydride state in the catalytic cycle of [FeFe]-hydrogenases. *Nat. Commun.* **2017**, *8*, 16115. [[CrossRef](#)] [[PubMed](#)]
24. Pelmenschikov, V.; Birrell, J.A.; Pham, C.C.; Mishra, N.; Wang, H.; Sommer, C.; Reijerse, E.; Richers, C.P.; Tamasaku, K.; Yoda, Y.; et al. Reaction coordinate leading to H₂ production in [FeFe]-hydrogenase identified by nuclear resonance vibrational spectroscopy and density functional theory. *J. Am. Chem. Soc.* **2017**, *139*, 16894–16902. [[CrossRef](#)]
25. Mulder, D.W.; Boyd, E.S.; Sarma, R.; Lange, R.K.; Endrizzi, J.A.; Broderick, J.B.; Peters, J.W. Stepwise [FeFe]-hydrogenase H-cluster assembly revealed in the structure of HydAΔEFG. *Nature* **2010**, *465*, 248–251. [[CrossRef](#)] [[PubMed](#)]
26. Esselborn, J.; Muraki, N.; Klein, K.; Engelbrecht, V.; Metzler-Nolte, N.; Apfel, U.P.; Hofmann, E.; Kurisu, G.; Happe, T. A structural view of synthetic cofactor integration into [FeFe]-hydrogenases. *Chem. Sci.* **2016**, *7*, 959–968. [[CrossRef](#)] [[PubMed](#)]
27. Lorent, C.; Katz, S.; Duan, J.; Kulka, C.J.; Caserta, G.; Teutloff, C.; Yadav, S.; Apfel, U.-P.; Winkler, M.; Happe, T.; et al. Shedding light on proton and electron dynamics in [FeFe] hydrogenases. *J. Am. Chem. Soc.* **2020**, *142*, 5493–5497. [[CrossRef](#)]
28. Sanchez, M.L.K.; Sommer, C.; Reijerse, E.; Birrell, J.A.; Lubitz, W.; Dyer, R.B. Investigating the kinetic competency of CrHydA1 [FeFe] hydrogenase intermediate states via time-resolved infrared spectroscopy. *J. Am. Chem. Soc.* **2019**, *141*, 16064–16070. [[CrossRef](#)] [[PubMed](#)]
29. Haumann, M.; Stripp, S.T. The molecular proceedings of biological hydrogen turnover. *Acc. Chem. Res.* **2018**, *51*, 1755–1763. [[CrossRef](#)]
30. Ratzloff, M.W.; Artz, J.H.; Mulder, D.W.; Collins, R.T.; Furtak, T.E.; King, P.W. CO-bridged H-cluster intermediates in the catalytic mechanism of [FeFe]-hydrogenase Cal. *J. Am. Chem. Soc.* **2018**, *140*, 7623–7628. [[CrossRef](#)]
31. De Lacey, A.L.; Stadler, C.; Cavazza, C.; Hatchikian, E.C.; Fernandez, V.M. FTIR characterization of the active site of the Fe-hydrogenase from *Desulfovibrio desulfuricans*. *J. Am. Chem. Soc.* **2000**, *122*, 11232–11233. [[CrossRef](#)]
32. Roseboom, W.; De Lacey, A.L.; Fernandez, V.M.; Hatchikian, E.C.; Albracht, S.P. The active site of the [FeFe]-hydrogenase from *Desulfovibrio desulfuricans*. II. Redox properties, light sensitivity and CO-ligand exchange as observed by infrared spectroscopy. *J. Biol. Inorg. Chem.* **2006**, *11*, 102–118. [[CrossRef](#)]
33. Rodríguez-Maciá, P.; Kertess, L.; Burnik, J.; Birrell, J.A.; Hofmann, E.; Lubitz, W.; Happe, T.; Rüdiger, O. His-ligation to the [4Fe-4S] subcluster tunes the catalytic bias of [FeFe] hydrogenase. *J. Am. Chem. Soc.* **2019**, *141*, 472–481. [[CrossRef](#)] [[PubMed](#)]
34. Rodríguez-Maciá, P.; Pawlak, K.; Rüdiger, O.; Reijerse, E.J.; Lubitz, W.; Birrell, J.A. Intercluster redox coupling influences protonation at the H-cluster in [FeFe] hydrogenases. *J. Am. Chem. Soc.* **2017**, *139*, 15122–15134. [[CrossRef](#)]
35. Sommer, C.; Adamska-Venkatesh, A.; Pawlak, K.; Birrell, J.A.; Rüdiger, O.; Reijerse, E.J.; Lubitz, W. Proton coupled electronic rearrangement within the H-cluster as an essential step in the catalytic cycle of [FeFe] hydrogenases. *J. Am. Chem. Soc.* **2017**, *139*, 1440–1443. [[CrossRef](#)] [[PubMed](#)]
36. Senger, M.; Laun, K.; Wittkamp, F.; Duan, J.; Haumann, M.; Happe, T.; Winkler, M.; Apfel, U.P.; Stripp, S.T. Proton-coupled reduction of the catalytic [4Fe-4S] cluster in [FeFe]-hydrogenases. *Angew. Chem. Int. Ed.* **2017**, *56*, 16503–16506. [[CrossRef](#)]
37. Rodríguez-Maciá, P.; Reijerse, E.; Lubitz, W.; Birrell, J.A.; Rüdiger, O. Spectroscopic evidence of reversible disassembly of the [FeFe] hydrogenase active site. *J. Phys. Chem. Lett.* **2017**, *8*, 3834–3839. [[CrossRef](#)]
38. Adamska-Venkatesh, A.; Krawietz, D.; Siebel, J.; Weber, K.; Happe, T.; Reijerse, E.; Lubitz, W. New redox states observed in [FeFe] hydrogenases reveal redox coupling within the H-cluster. *J. Am. Chem. Soc.* **2014**, *136*, 11339–11346. [[CrossRef](#)]
39. Nernst, W.J. Die elektromotorische wirksamkeit der jonen. *Z. Phys. Chem.* **1889**, *4*, 129–181. [[CrossRef](#)]
40. Delahay, P.; Pourbaix, M.; Van Rysselberghe, P. Potential-pH diagrams. *J. Chem. Ed.* **1950**, *27*, 683. [[CrossRef](#)]
41. Adamska, A.; Silakov, A.; Lambert, C.; Rüdiger, O.; Happe, T.; Reijerse, E.; Lubitz, W. Identification and characterization of the “super-reduced” state of the H-cluster in [FeFe] hydrogenase: A new building block for the catalytic cycle? *Angew. Chem. Int. Ed.* **2012**, *51*, 11458–11462. [[CrossRef](#)] [[PubMed](#)]
42. Silakov, A.; Kamp, C.; Reijerse, E.; Happe, T.; Lubitz, W. Spectroelectrochemical characterization of the active site of the [FeFe] hydrogenase HydA1 from *Chlamydomonas reinhardtii*. *Biochemistry* **2009**, *48*, 7780–7786. [[CrossRef](#)]

43. Katz, S.; Noth, J.; Horch, M.; Shafaat, H.S.; Happe, T.; Hildebrandt, P.; Zebger, I. Vibrational spectroscopy reveals the initial steps of biological hydrogen evolution. *Chem. Sci.* **2016**, *7*, 6746–6752. [[CrossRef](#)]
44. Lampret, O.; Duan, J.; Hofmann, E.; Winkler, M.; Armstrong, F.A.; Happe, T. The roles of long-range proton-coupled electron transfer in the directionality and efficiency of [FeFe]-hydrogenases. *Proc. Natl. Acad. Sci. USA* **2020**, *117*, 20520–20529. [[CrossRef](#)]
45. Kertess, L.; Adamska-Venkatesh, A.; Rodríguez-Maciá, P.; Rüdiger, O.; Lubitz, W.; Happe, T. Influence of the [4Fe-4S] cluster coordinating cysteines on active site maturation and catalytic properties of *C. reinhardtii* [FeFe]-hydrogenase. *Chem. Sci.* **2017**, *8*, 8127–8137. [[CrossRef](#)] [[PubMed](#)]
46. Léger, C.; Bertrand, P. Direct electrochemistry of redox enzymes as a tool for mechanistic studies. *Chem. Rev.* **2008**, *108*, 2379–2438. [[CrossRef](#)] [[PubMed](#)]
47. Pandey, K.; Islam, S.T.A.; Happe, T.; Armstrong, F.A. Frequency and potential dependence of reversible electrocatalytic hydrogen interconversion by [FeFe]-hydrogenases. *Proc. Natl. Acad. Sci. USA* **2017**, *114*, 3843–3848. [[CrossRef](#)]
48. Artz, J.H.; Zadovornyy, O.A.; Mulder, D.W.; Keable, S.M.; Cohen, A.E.; Ratzloff, M.W.; Williams, S.G.; Ginovska, B.; Kumar, N.; Song, J.; et al. Tuning catalytic bias of hydrogen gas producing hydrogenases. *J. Am. Chem. Soc.* **2020**, *142*, 1227–1235. [[CrossRef](#)]
49. Caserta, G.; Papini, C.; Adamska-Venkatesh, A.; Pecqueur, L.; Sommer, C.; Reijerse, E.; Lubitz, W.; Gauquelin, C.; Meynial-Salles, I.; Pramanik, D.; et al. Engineering an [FeFe]-hydrogenase: Do accessory clusters influence O₂ resistance and catalytic bias? *J. Am. Chem. Soc.* **2018**, *140*, 5516–5526. [[CrossRef](#)] [[PubMed](#)]
50. Gauquelin, C.; Baffert, C.; Richaud, P.; Kamionka, E.; Etienne, E.; Guieysse, D.; Girbal, L.; Fourmond, V.; André, I.; Guigliarelli, B.; et al. Roles of the F-domain in [FeFe] hydrogenase. *Biochim. Biophys. Acta Bioenerg.* **2018**, *1859*, 69–77. [[CrossRef](#)]
51. Rodríguez-Maciá, P.; Breuer, N.; DeBeer, S.; Birrell, J.A. Insight into the redox behavior of the [4Fe-4S] subcluster in [FeFe] hydrogenases. *ACS Catal.* **2020**, *10*, 13084–13095. [[CrossRef](#)]
52. Can, M.; Armstrong, F.A.; Ragsdale, S.W. Structure, function, and mechanism of the nickel metalloenzymes, CO dehydrogenase, and acetyl-CoA synthase. *Chem. Rev.* **2014**, *114*, 4149–4174. [[CrossRef](#)] [[PubMed](#)]
53. Amara, P.; Mouesca, J.M.; Volbeda, A.; Fontecilla-Camps, J.C. Carbon monoxide dehydrogenase reaction mechanism: A likely case of abnormal CO₂ insertion to a Ni-H bond. *Inorg. Chem.* **2011**, *50*, 1868–1878. [[CrossRef](#)] [[PubMed](#)]
54. Caserta, G.; Lorent, C.; Ciaccafava, A.; Keck, M.; Breglia, R.; Greco, C.; Limberg, C.; Hildebrandt, P.; Cramer, S.P.; Zebger, I.; et al. The large subunit of the regulatory [NiFe]-hydrogenase from *Ralstonia eutropha*—A minimal hydrogenase? *Chem. Sci.* **2020**, *11*, 5453–5465. [[CrossRef](#)]
55. Seefeldt, L.C.; Yang, Z.-Y.; Lukoyanov, D.A.; Harris, D.F.; Dean, D.R.; Raugei, S.; Hoffman, B.M. Reduction of substrates by nitrogenases. *Chem. Rev.* **2020**, *120*, 5082–5106. [[CrossRef](#)]
56. Van Stappen, C.; Decamps, L.; Cutsail, G.E.; Bjornsson, R.; Henthorn, J.T.; Birrell, J.A.; DeBeer, S. The spectroscopy of nitrogenases. *Chem. Rev.* **2020**, *120*, 5005–5081. [[CrossRef](#)] [[PubMed](#)]
57. Rutledge, H.L.; Tezcan, F.A. Electron transfer in nitrogenase. *Chem. Rev.* **2020**, *120*, 5158–5193. [[CrossRef](#)]